

# Sliding Dynamics of Skyrmion Molecular Crystals

J. C. Bellizotti Souza<sup>1,\*</sup>, C. J. O. Reichhardt<sup>2</sup>, C. Reichhardt<sup>2</sup>, N. P. Vizarim<sup>3</sup> and P. A. Venegas<sup>4</sup>

E-mail: [jc.souza@unesp.br](mailto:jc.souza@unesp.br)

\* Corresponding author

<sup>1</sup> POSMAT - Programa de Pós-Graduação em Ciência e Tecnologia de Materiais, São Paulo State University (UNESP), School of Sciences, Bauru 17033-360, SP, Brazil

<sup>2</sup> Theoretical Division and Center for Nonlinear Studies, Los Alamos National Laboratory, Los Alamos, New Mexico 87545, USA

<sup>3</sup> “Gleb Wataghin” Institute of Physics, University of Campinas, 13083-859 Campinas, São Paulo, Brazil

<sup>4</sup> Department of Physics, São Paulo State University (UNESP), School of Sciences, Bauru 17033-360, SP, Brazil

**Abstract.** Using both atomistic and particle-based simulations, we investigate the current-driven dynamics of skyrmions on two-dimensional periodic substrates when there are multiple skyrmions per substrate minimum. At zero drive, the system forms pinned skyrmion molecular crystal states consisting of dimers, trimers, or dimer-trimer mixtures that have both positional and orientational order. On a square substrate lattice, the motion above depinning occurs via a running soliton that travels completely transverse to the applied current. This motion is generated by a torque from the Magnus force, which rotates the  $n$ -mer states perpendicular to the applied current. At higher drives, the flow becomes disordered while the Hall angle diminishes and gradually approaches the intrinsic value. In some cases, we also find directional locking where the Hall angle becomes locked to certain symmetry directions of the substrate over a range of currents. The transitions into and out of directionally locked states are accompanied by negative differential mobility in which the net velocity decreases as the drive increases. On a triangular substrate, we find no transverse mobility effects, but still observe directionally locked motion.

## 1. Introduction

There are a variety of systems that can be effectively described as interacting particles coupled to a two-dimensional periodic substrate, and in these systems, the interparticle interactions favor a certain spacing that may differ from the energy-minimizing spacing imposed by the substrate. Under these conditions, commensurate-incommensurate transitions can occur as the ratio of the number of particles to the number of substrate minima is varied [1, 2, 3, 4, 5]. For commensurate conditions, the number of particles is an integer multiple of the number of substrate minima, such as a one-to-one matching. At incommensurate fillings, the system still forms an ordered structure but contains interstitials or vacancies that act as kinks or antikinks [1, 4]. In some cases, the density of incommensurations is high enough to cause the system to disorder. Ordered commensurate states can also appear for fractional fillings such as  $1/2$  or  $1/3$  [6, 7, 8, 9]. Under an applied drive, the threshold force needed to depin the particles is maximized at the commensurate conditions, and a single depinning transition occurs. At incommensurate fillings, the depinning threshold can be dramatically reduced and can also occur via a multistep process in which the kinks or antikinks begin to slide first, followed by the sliding of the remaining particles at higher drives [5].

Commensurate-incommensurate transitions have been studied for the ordering of atoms and molecules on periodic surfaces [1, 2], vortices in type-II superconductors with artificial periodic pinning arrays [10, 3, 7, 8, 9], vortices in Bose-Einstein condensates on optical trap arrays [11], charged colloids on optical traps or patterned substrates [12, 13, 14, 4], dusty plasmas [15], liquid crystal skyrmions on ordered substrates [16] and generalized Wigner crystals for charge ordering on periodic substrates in moiré systems [17, 18]. Most studies of commensurate-incommensurate systems have been performed for one or slightly more than one particle per substrate minimum. In superconducting vortex systems, at commensurate fillings for which there are two or more vortices per trap, the individual vortices can merge to form multiquantum vortices [10]. There can also be situations for which the trapped particles are unable to merge, and the system contains  $n$  separate particles per trap. In this case, each substrate minimum contains an  $n$ -mer state that has positional ordering produced by the substrate periodicity. The  $n$ -mers may also exhibit an additional orientational ordering with the other  $n$ -mers [19, 12, 20, 21, 22, 23, 24, 25].

When multiple colloidal particles are trapped by each substrate potential minimum in an optical trap array, the ordered states are called colloidal molecular crystals [19, 12, 20, 21]. For fillings  $N = 2.0$ , the colloids form dimers that can arrange into herringbone lattices where the tilt angle of the dimers alternates from one row to the next, antiferromagnetic lattices in which adjacent dimers are perpendicular to each other, or ferromagnetic states in which all of the dimers have the same alignment. Trimers can also exhibit ferromagnetic and columnar ordering depending on the substrate symmetry and strength [19, 12, 20, 21]. As a function of increasing temperature or changing colloidal interaction strength, the molecular crystals can undergo a transition from an orientationally ordered to an orientationally disordered state in which each substrate minimum still contains  $n$  particles that form an  $n$ -mer, but the global orientational ordering of the  $n$ -mers is lost [19, 12, 20, 21]. At higher temperatures, the system forms a modulated liquid in which colloidal particles can hop among the substrate minima [19, 12, 26, 22]. More recently, Wigner crystal molecule crystals were observed for charge ordering of two or more electrons per trap on ordered substrates [27].

There have also been studies of colloidal molecular crystal mixtures at fillings of  $3/2$  and  $5/2$  in which monomer-dimer or dimer-trimer mixtures are present that create larger scale superlattice orderings [22]. Recently, magnetic skyrmion molecular crystals were proposed for skyrmions interacting with periodic two-dimensional substrates when two or more skyrmions per substrate minimum are present [28]. Such states could arise for skyrmions in moiré materials [29] or skyrmions in systems with ordered nanostructures, such as from patterned irradiation or surface modulation [30]. Skyrmion molecular crystals are distinct from particle-based molecular crystals in that the skyrmions can distort or annihilate, making it possible for ordered lattices to occur in which the skyrmions have different sizes in the same trap, are stretched into meron pairs, or partially annihilate to make the state more ordered [28].

In particle-based systems, driven colloidal molecular crystals have been shown to exhibit a variety of moving phases, and transitions between the different flow phases can be correlated with features in the velocity-force curves [31, 32]. The dynamic states include plastic flow phases, where some particles move while others remain pinned, fluid-like flows, and moving crystal phases. An open question is whether the dynamics of the deformable skyrmion molecular crystal states are similar or different from the dynamics observed for rigid colloidal molecular crystal states.

Skyrmions are particle-like magnetic textures that can form a triangular lattice [33, 34, 35], and be set into motion by an applied spin current [36, 37]. When they interact with defects or interfaces, pinning effects can arise and there can be a finite threshold current for motion [38]. A key feature that distinguishes skyrmion dynamics from the dynamics of most other systems is that skyrmions have a strong non-dissipative Magnus force component to their motion [35, 39, 38]. The Magnus force causes skyrmions to have a finite Hall angle with respect to an external drive and also affects how the skyrmions interact with interfaces, pinning, and other skyrmions [40, 41, 42, 38]. For skyrmions interacting with pinning sites, the Magnus force generates a spiraling motion that can reduce the pinning effectiveness or modify the Hall angle [43, 38]. The skyrmion Hall angle becomes strongly drive dependent in the presence of pinning, starting from a value of nearly zero at low drives just above depinning and then increasing as the drive increases [44, 40, 41]. The pinning reduces the Hall angle by inducing a side jump of the skyrmions as they move over the pinning sites, and the size of this side jump diminishes with increasing drive so that at high drives, the skyrmion travels along a direction close to the intrinsic skyrmion Hall angle [38]. In a particle-based model, the motion of a single skyrmion driven with an increasing current over a periodic substrate shows a directional locking effect in which the skyrmion Hall angle increases in a series of steps as the skyrmion motion becomes locked to specific symmetry directions of the substrate over an interval of drives. For a square array, the motion is most strongly locked along  $45^\circ$ , but weaker locking occurs for other angles  $\theta = \arctan(n/m)$ , where  $n$  and  $m$  are integers. For a triangular substrate, the strongest directional locking occurs along  $60^\circ$  [45, 46]. This directional locking effect also occurs for overdamped particles such as vortices and colloids moving over a periodic substrate; however, in those systems the direction, and not merely the magnitude, of the drive must be varied [47, 48, 49, 50].

In studies of skyrmions driven over a quasi-one-dimensional substrate when the number of skyrmions is just above or below the first matching filling [51], the depinning occurs through the motion of soliton kink at a lower drive. The other skyrmions depin at a higher drive, leading to a two-step depinning process. For skyrmions on two-dimensional substrates just above or below the first matching filling, depinning also

occurs by kink or anti-kink flow in which directional locking of the kinks is possible [52]. Both atomistic and particle-based models of this process produce the same dynamic phases, but give quantitative differences due to the ability of the skyrmions to distort only in the atomistic model.

Here, we use atomistic and particle-based simulations to examine the dynamics of skyrmion molecular crystals for fillings of  $N_{\text{sk}}/N_m = 3/2, 2.0, 5/2,$  and  $3.0$  on square and triangular substrates, where  $N_{\text{sk}}$  is the number of skyrmions and  $N_m$  is the number of substrate minima. Previous work explored only the static ordering of skyrmions on triangular substrates [28]. For square substrates at a filling of  $N_{\text{sk}}/N_m = 2.0$ , the system forms dimers with antiferromagnetic ordering, similar to the ordering found in colloidal molecular crystals on square lattices [19, 20]. For  $N_{\text{sk}}/N_m = 3.0$ , trimers appear that form a columnar ordered phase, while the  $N_{\text{sk}}/N_m = 1.5$  and  $N_{\text{sk}}/N_m = 2.5$  systems form monomer-dimer and dimer-trimer mixtures, respectively. We consider a system with an intrinsic Hall angle of  $\theta_{\text{int}} = 26^\circ$ . For the square substrates, depinning of the dimers and trimers occurs into a state where the flow is perpendicular to the current with a Hall angle of  $\theta = 90^\circ$ . At higher drives, the Hall angle gradually decreases toward  $\theta_{\text{int}}$ . We also find directional locking to  $45^\circ$ , one of the symmetry directions of the square substrate. The transitions into and out of the directionally locked states are associated with negative differential mobility in which the net velocity decreases with increasing drive [38]. For a filling of  $N_{\text{sk}}/N_m = 3/2$ , where a mixture of dimers and monomers is present, the absolute transverse mobility is lost, but there is strong directional locking along  $45^\circ$  in which solitons flow along rows with dimers while monomer rows remain pinned. At  $N_{\text{sk}}/N_m = 5/2$  where there is a dimer-trimer mixture, we find a region of absolute transverse mobility accompanied at each end by negative differential mobility. For triangular substrates, absolute transverse motion does not occur, but motion above the initial depinning transition runs close to  $60^\circ$  along a substrate symmetry direction. Generally, the depinning threshold is much higher for triangular substrates than for square substrates. We observe the same phases with a particle-based model but find some quantitative differences between the two models.

## 2. Methods

### 2.1. Atomistic simulations

Atomistic simulations capture the dynamics of individual atomic magnetic moments [53]. We model a ferromagnetic ultrathin film capable of holding Néel skyrmions. Our sample has dimensions of  $84 \text{ nm} \times 84 \text{ nm}$  with periodic boundary conditions along the  $x$  and  $y$  directions. We apply a magnetic field perpendicular to the sample along the  $-z$  direction and work at zero temperature,  $T = 0 \text{ K}$ .

The Hamiltonian governing the atomistic dynamics is given by [37, 53, 54]:

$$\begin{aligned} \mathcal{H} = & - \sum_{\langle i,j \rangle} J_{ij} \mathbf{m}_i \cdot \mathbf{m}_j - \sum_{\langle i,j \rangle} \mathbf{D}_{ij} \cdot (\mathbf{m}_i \times \mathbf{m}_j) \\ & - \sum_i \mu \mathbf{H} \cdot \mathbf{m}_i - \sum_i K(x_i, y_i) (\mathbf{m}_i \cdot \hat{\mathbf{z}})^2 . \end{aligned} \quad (1)$$

The ultrathin film is modeled as a square arrangement of atoms with a lattice constant  $a = 0.5 \text{ nm}$ . The first term on the right hand side is the exchange interaction

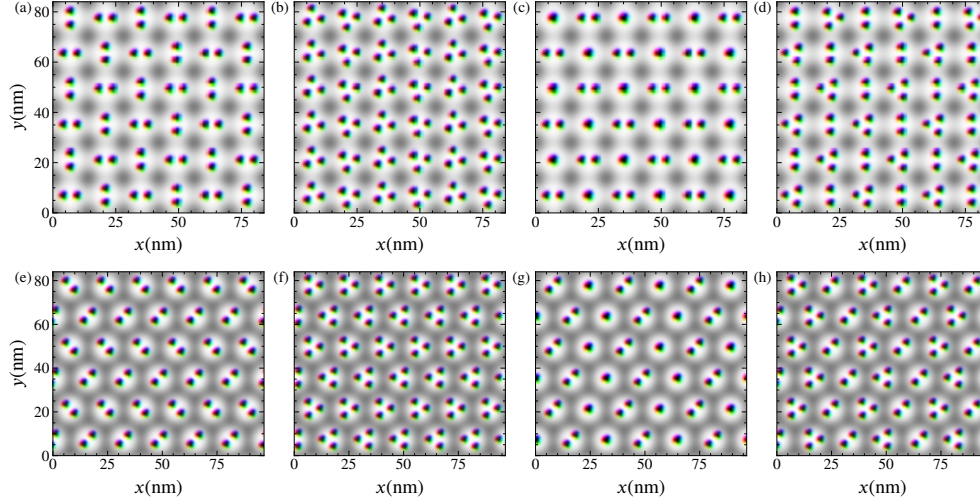


**Figure 1.** Different skyrmion arrangements for skyrmions on (a-d) square and (e-h) triangular substrates from an atomistic model. The sample perpendicular magnetic anisotropy (PMA) is represented by a gray overlay, where darker areas have higher PMA and brighter areas have lower PMA. (a) Antiferromagnetic and (e) herringbone dimer ordering at  $N_{\text{sk}}/N_m = 2$ . (b, f) Alternating column trimer arrangement at  $N_{\text{sk}}/N_m = 3$ . (c, g) Bipartite monomer-dimer arrangement with ferromagnetically aligned dimers at  $N_{\text{sk}}/N_m = 3/2$ . (d, h) Bipartite dimer-trimer 5/2 arrangement at  $N_{\text{sk}}/N_m = 5/2$ .

with an exchange constant of  $J_{ij} = J$  between magnetic moments  $i$  and  $j$ . The second term is the interfacial Dzyaloshinskii–Moriya interaction, where  $\mathbf{D}_{ij} = D\hat{\mathbf{z}} \times \hat{\mathbf{r}}_{ij}$  is the Dzyaloshinskii–Moriya vector between magnetic moments  $i$  and  $j$  and  $\hat{\mathbf{r}}_{ij}$  is the unit distance vector between sites  $i$  and  $j$ . Here,  $\langle i, j \rangle$  indicates that the sum is over only the first neighbors of the  $i$ th magnetic moment. The third term is the Zeeman interaction with an applied external magnetic field  $\mathbf{H}$ . Here  $\mu = g\mu_B$  is the magnitude of the magnetic moment,  $g = |g_e| = 2.002$  is the electron  $g$ -factor, and  $\mu_B = 9.27 \times 10^{-24} \text{ J T}^{-1}$  is the Bohr magneton. The last term represents the sample perpendicular magnetic anisotropy (PMA), where  $x_i$  and  $y_i$  are the spatial coordinates of the  $i$ th magnetic moment. In ultrathin films, long-range dipolar interactions act as a PMA (see Supplemental of Wang *et al.* [55]), and therefore merely effectively shift the PMA values.

The time evolution of atomic magnetic moments is obtained using the Landau-Lifshitz-Gilbert (LLG) equation [56, 57]:

$$\frac{\partial \mathbf{m}_i}{\partial t} = -\gamma \mathbf{m}_i \times \mathbf{H}_i^{\text{eff}} + \alpha \mathbf{m}_i \times \frac{\partial \mathbf{m}_i}{\partial t} + \frac{pa^3}{2e} (\mathbf{j} \cdot \nabla) \mathbf{m}_i. \quad (2)$$

Here  $\gamma = 1.76 \times 10^{11} \text{ T}^{-1} \text{ s}^{-1}$  is the electron gyromagnetic ratio,  $\mathbf{H}_i^{\text{eff}} = -\frac{1}{\mu} \frac{\partial \mathcal{H}}{\partial \mathbf{m}_i}$  is the effective magnetic field including all interactions from the Hamiltonian,  $\alpha$  is the phenomenological damping introduced by Gilbert, and the last term is the adiabatic spin-transfer-torque (STT) caused by application of an in plane spin polarized current, where  $p$  is the spin polarization,  $e$  the electron charge, and  $\mathbf{j} = j\hat{\mathbf{x}}$  the applied current density. Use of this STT expression implies that the conduction electron spins are always parallel to the magnetic moments  $\mathbf{m}$ [37, 58].

In this work we consider two anisotropy patterns, a square substrate given by

$$K_S(x, y) = \frac{K_0}{4} \left[ \cos\left(\frac{2\pi x}{a_0}\right) + \cos\left(\frac{2\pi y}{a_0}\right) + 2 \right], \quad (3)$$

and a triangular substrate given by

$$K_T(x, y) = \frac{2K_0}{9} \left[ 3 + \sum_{i=1}^3 \cos\left(\frac{2\pi b_i}{a_0}\right) \right], \quad (4)$$

where  $K_0$  is the anisotropy depth and  $a_0 = 14$  nm is the substrate lattice constant for both patterns. In the triangular pattern,  $b_i = x \cos \theta_i - y \sin \theta_i + a_0/2$  with  $\theta_1 = \pi/6$ ,  $\theta_2 = \pi/2$  and  $\theta_3 = 5\pi/6$ . Both patterns produce anisotropies falling in the range  $0 \leq K(x, y) \leq K_0$ , and both the square and triangular substrates have a total of  $N_m = 36$  anisotropy minima. For the triangular substrate, we change the sample dimensions to 96.5 nm  $\times$  84 nm in order to properly apply the periodic boundary conditions.

The skyrmion velocity is computed using the emergent electromagnetic fields [56, 59]:

$$E_i^{\text{em}} = \frac{\hbar}{e} \mathbf{m} \cdot \left( \frac{\partial \mathbf{m}}{\partial i} \times \frac{\partial \mathbf{m}}{\partial t} \right) \quad (5)$$

$$B_i^{\text{em}} = \frac{\hbar}{2e} \varepsilon_{ijk} \mathbf{m} \cdot \left( \frac{\partial \mathbf{m}}{\partial j} \times \frac{\partial \mathbf{m}}{\partial k} \right), \quad (6)$$

where  $\varepsilon_{ijk}$  is the totally anti-symmetric tensor. The skyrmion drift velocity,  $\mathbf{v}_d$ , is then calculated using  $\mathbf{E}^{\text{em}} = -\mathbf{v}_d \times \mathbf{B}^{\text{em}}$ . The skyrmion Hall angle is computed using  $\theta = \arctan(\langle v_y \rangle / \langle v_x \rangle)$

We fix the following values in our simulations:  $\mu\mathbf{H} = 0.6(D^2/J)(-\hat{\mathbf{z}})$ ,  $\alpha = 0.3$ , and  $p = -1.0$ . The material parameters are  $J = 1$  meV,  $D = 0.5J$ , and  $K_0 = 0.2J$  unless otherwise mentioned. For each simulation, the system is initialized in one of the configurations illustrated in Fig. 1. The numerical integration of Eq. 2 is performed using a fourth order Runge-Kutta method over 200 ns.

In our system, we consider STTs that create a force perpendicular to the current direction. Thus, just at depinning, when the skyrmions travel in the direction of the driving force they have a Hall angle of  $90^\circ$ , which decreases to the intrinsic value at higher drives. When we perform simulations on a clean sample, we find that the skyrmions move at  $\theta_{\text{sk}}^{\text{int}} = 26^\circ$  with respect to the current, which corresponds to an angle of  $\theta = 64^\circ$  with respect to the driving force.

## 2.2. Particle based simulations

We also simulate the particle based model developed by Lin *et al.* [60]. The equation of motion governing the dynamics is given by

$$\alpha_d \mathbf{v}_i + \alpha_m \hat{\mathbf{z}} \times \mathbf{v}_i = \sum_{i \neq j} \mathbf{F}_{\text{sk}}(\mathbf{r}_{ij}) + \mathbf{F}_{\text{P}}(\mathbf{r}_i) + \hat{\mathbf{z}} \times \mathbf{F}_D, \quad (7)$$

where  $\mathbf{v}_i$  is the velocity of skyrmion  $i$ . The first term on the left is the damping term of strength  $\alpha_d$ . The second term is the Magnus force of strength  $\alpha_m$ . The intrinsic Hall angle is given by  $\theta_{\text{sk}}^{\text{int}} = \arctan(\alpha_m/\alpha_d)$ . In order to match the particle based simulations with our atomistic based simulations, we performed atomistic simulations

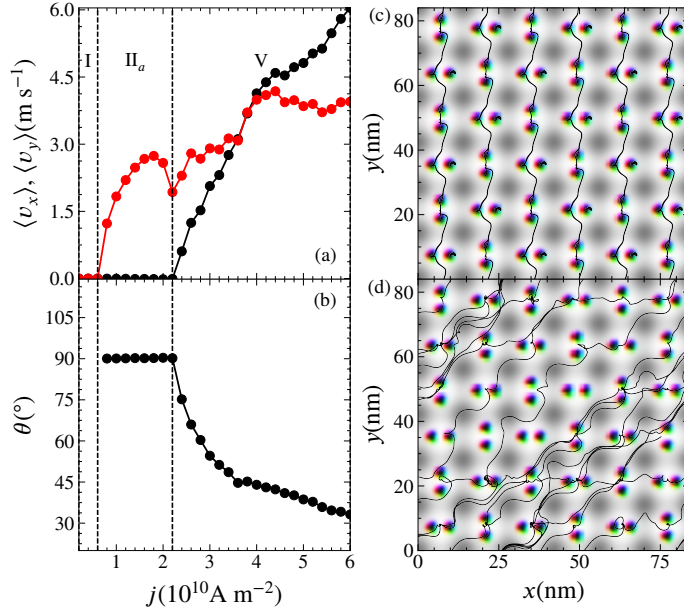


**Figure 2.** (a) Average skyrmion velocities  $\langle v_x \rangle$  (black) and  $\langle v_y \rangle$  (red) and (b) the corresponding skyrmion Hall angle  $\theta$  vs applied current  $j$  from an atomistic model for the dimer  $N_{\text{sk}}/N_m = 2.0$  filling on a square substrate shown in Fig. 1(a). I: pinned phase.  $\text{II}_a$ :  $90^\circ$  transverse motion. V: partially disordered motion. (c, d) Skyrmion trajectories at representative drives for the same system. (c) Trajectories of all skyrmions in phase  $\text{II}_a$  at  $j = 1.4 \times 10^{10} \text{ A m}^{-2}$ . (d) Trajectory of a single skyrmion in phase V at  $j = 5 \times 10^{10} \text{ A m}^{-2}$ .

on clean samples and obtained an intrinsic Hall angle of  $\theta_{\text{sk}}^{\text{int}} = 26^\circ$ ; this value was then used to determine the values of  $\alpha_m = \sin(64^\circ)$  and  $\alpha_d = \cos(64^\circ)$  based on the fact that the skyrmions move with an angle of  $64^\circ$  with respect to the driving force. The first term on the right side of Eq. 7 is the skyrmion-skyrmion interaction, given by  $\mathbf{F}_{\text{sk}}(\mathbf{r}_{ij}) = -U_{\text{sk}}K_1(r_{ij})\hat{\mathbf{r}}_{ij}$ , where  $U_{\text{sk}} = 1$  is the interaction strength and  $K_1$  is the modified first order Bessel function. The second term is the interaction with the underlying substrate potential, represented by the same equations, Eqs. 3 and 4, as in the atomistic model, with the adjustment  $K_0 \rightarrow A$  where  $A = 0.75$ . By taking  $a_0 = 6$  we obtain substrates with  $N_m = 36$  potential minima. The last term is the interaction with an external drive,  $\mathbf{F}_D = F_D \hat{\mathbf{x}}$ , corresponding to the action of an STT current on magnetic skyrmions [37, 39, 61]. Our simulation box is of size  $36 \times 36$  with periodic boundary conditions along the  $x$  and  $y$  directions. The sample size is adjusted to  $36(2/\sqrt{3}) \times 36$  for the triangular substrate in order to properly apply the periodic boundary conditions.

### 3. Dynamics of Skyrmion Molecular Crystals on Square Substrates

We first consider atomistic simulations of skyrmions on a square substrate, illustrated in Fig. 1(a-d). At  $N_{\text{sk}}/N_m = 2$  in Fig. 1(a), the skyrmions form dimers with the dimer center located at the trap minimum. Adjacent dimers are perpendicular to each other forming what we describe as antiferromagnetic ordering, which is similar

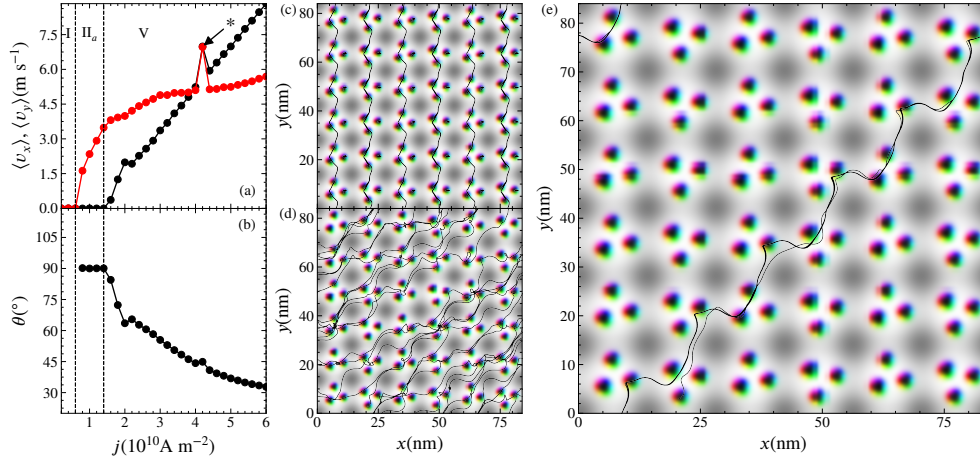


**Figure 3.** (a) Average skyrmion velocities  $\langle v_x \rangle$  (black) and  $\langle v_y \rangle$  (red) and (b) the corresponding skyrmion Hall angle  $\theta$  vs  $j$  from an atomistic model for the trimer  $N_{\text{sk}}/N_m = 3.0$  filling on a square substrate shown in Fig. 1(b). I: pinned phase. II<sub>a</sub>:  $90^\circ$  transverse motion. V: partially disordered motion. The \* symbol indicates the point at  $j = 4.2 \times 10^{10} \text{ A m}^{-2}$  where the velocities peak and the motion is directionally locked along  $45^\circ$ . (c, d, e) Skyrmion trajectories at representative drives for the same system. (c) Trajectories of all skyrmions in phase II<sub>a</sub> at  $j = 1 \times 10^{10} \text{ A m}^{-2}$ . (d) Trajectory of a single skyrmion in phase V at  $j = 5 \times 10^{10} \text{ A m}^{-2}$ . (e) Trajectory of a single skyrmion in phase V at  $j = 4.2 \times 10^{10} \text{ A m}^{-2}$ , the directionally locked current marked by a \* in panel (a).

to the ordering observed for dimerized colloidal particles on a square substrate [19, 20]. The colloidal particles interact with a short-range repulsion, and in that system the antiferromagnetic arrangement arises due to minimization of an effective quadrupole moment of the adjacent dimers [20]. Skyrmions can also be treated as repulsive particles, so they form a structure similar to that found for the colloidal system. At  $N_{\text{sk}}/N_m = 3$  in Fig. 1(b), trimers form with an orientation that alternates from one column to the next. Figure 1(c) shows a bipartite state at  $N_{\text{sk}}/N_m = 3/2$ , where an alternating mixture of monomers and dimers is present. Here, all of the dimers are aligned and exhibit ferromagnetic ordering. Similarly, at  $N_{\text{sk}}/N_m = 5/2$  in Fig. 1(d), in an alternating arrangement of dimers and trimers, the dimers are all aligned with each other and the trimers are also aligned with a slight tilt. Previous studies of skyrmion molecular crystals were performed for skyrmions coupled to a triangular substrate. We observe similar orderings as shown in Figs. 1(e-h). At  $N_{\text{sk}}/N_m = 2$  and  $N_{\text{sk}}/N_m = 3$ , the tilt angles of the dimers and trimers in Fig. 1(e) and (f), respectively, alternate from site to site, while the dimers in both the  $N_{\text{sk}}/N_m = 3/2$  and  $N_{\text{sk}}/N_m = 5/2$  states in Fig. 1(g) and (h) have ferromagnetic or aligned ordering. As we vary the filling, we find many other states beyond those illustrated in Fig. 1, which we will describe in a future work.

In Fig. 2(a) we plot the average skyrmion velocities  $\langle v_x \rangle$  and  $\langle v_y \rangle$  versus current  $j$  for the  $N_{\text{sk}}/N_m = 2$  dimer system from Fig. 1(a), and in Fig. 2(b) we show the corresponding Hall angle  $\theta$  versus  $j$ . In the absence of a substrate, the skyrmions would flow at  $\theta = 26^\circ$ . We find that for  $j \leq 0.6 \times 10^{10} \text{ A m}^{-2}$ , the skyrmions are pinned, which we label region I in Fig. 2(a). The initial depinning occurs into a state where  $\langle v_y \rangle$



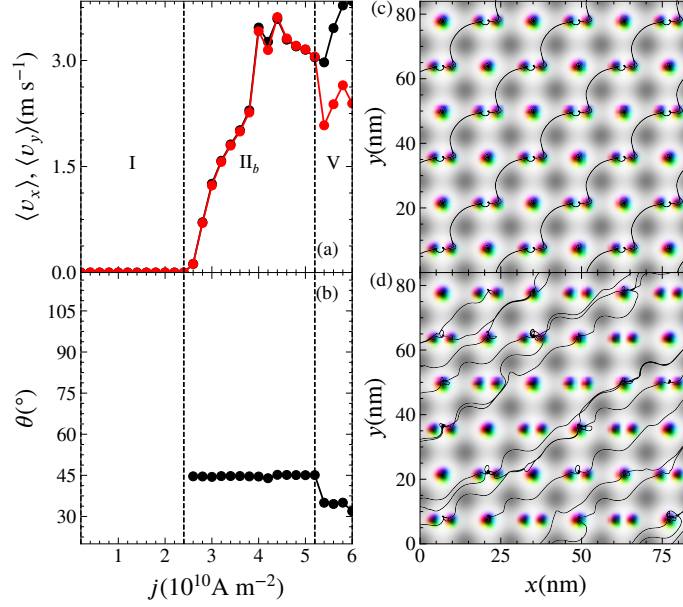


**Figure 4.** Average skyrmion velocities  $\langle v_x \rangle$  (black) and  $\langle v_y \rangle$  (red) and (b) the corresponding skyrmion Hall angle  $\theta$  vs  $j$  from an atomistic model for the monomer-dimer lattice at  $N_{\text{sk}}/N_m = 3/2$  on a square substrate from Fig. 1(c). I: pinned phase. II<sub>b</sub>: 45° directionally locked motion. V: partially disordered motion with no locking. (c, d) Skyrmion trajectories at representative drives for the same system. (c) Trajectories of all skyrmions in phase II<sub>b</sub> at  $j = 3 \times 10^{10} \text{ A m}^{-2}$ . (d) Trajectory of a single skyrmion in phase V at  $j = 6 \times 10^{10} \text{ A m}^{-2}$ .

increases with increasing  $j$  but  $\langle v_x \rangle = 0.0$ , indicating that the flow is perpendicular to the current. This transverse motion appears when  $0.6 \times 10^{10} \text{ A m}^{-2} < j \leq 2.2 \times 10^{10} \text{ A m}^{-2}$ , which we label region II<sub>a</sub>. As  $j$  increases further,  $\langle v_x \rangle$  begins to increase and  $\theta$  decreases from 90° toward the intrinsic Hall angle value of 26°. We label this region V flow. There is small window in which  $\langle v_x \rangle$  and  $\langle v_y \rangle$  are locked together, corresponding to directional locking along 45°, the major symmetry direction of the square substrate. Just below the transition from region II<sub>a</sub> to region V,  $\langle v_y \rangle$  decreases with increasing  $j$ , indicating negative differential mobility. A similar velocity dip has been observed at dynamic transitions for vortex flow in superconductors with periodic pinning [5], as well as for a single skyrmion moving over a periodic substrate at transitions into and out of certain symmetry locking directions [45].

In Fig. 2(c) we illustrate the skyrmion locations and trajectories in phase II<sub>a</sub> at  $j = 1.4 \times 10^{10} \text{ A m}^{-2}$ , where flow occurs via soliton motion in which an individual skyrmion jumps from one well to the next and triggers the jump of another single skyrmion. When the skyrmion jumps into a well with a dimer that is aligned along the  $x$  direction, the dimer rotates into the  $y$  direction and the upper skyrmion jumps out of the well. If the dimer is already aligned in the  $y$  direction before the arrival of the jumping skyrmion, the upper skyrmion jumps into the next well and no rotation occurs. At higher drives, the system enters phase V where the flow is more disordered and occurs along both the  $x$  and  $y$  directions. The phase V motion is shown in Fig. 2(d) at  $j = 5 \times 10^{10} \text{ A m}^{-2}$ , where we draw only one skyrmion trajectory for

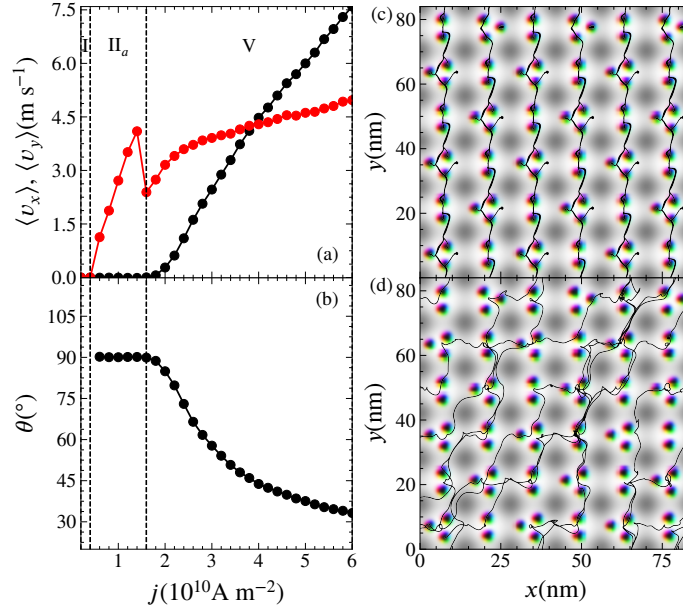


**Figure 5.** Average skyrmion velocities  $\langle v_x \rangle$  (black) and  $\langle v_y \rangle$  (red) and (b) the corresponding skyrmion Hall angle  $\theta$  vs  $j$  from an atomistic model for the dimer-trimer  $N_{\text{sk}}/N_m = 5/2$  filling on a square substrate from Fig. 1(d). I: pinned phase.  $\text{II}_a$ :  $90^\circ$  transverse motion. V: partially disordered motion. (c, d) Skyrmion trajectories at representative drives for the same system. (c) Trajectories of all skyrmions in phase  $\text{II}_a$  at  $j = 1 \times 10^{10} \text{ A m}^{-2}$ . (d) Trajectory of a single skyrmion in phase V at  $j = 3 \times 10^{10} \text{ A m}^{-2}$ .

clarity. Temporary locking motion along  $45^\circ$  is intermingled with more disordered flow, and some of the dimers remain pinned. As the drive increases, more of the dimers participate in the flow, which gradually rotates into a direction closer to that of the intrinsic Hall angle. In a sample just off commensuration, where a few skyrmions are removed or added, we find a similar trend in which the angle of skyrmion motion is initially large and then decreases as the drive increases; however, the presence of vacancies or interstitials produces much stronger directional locking of the flow compared to the commensurate case [52].

Figure 3(a,b) shows the average velocities  $\langle v_x \rangle$  and  $\langle v_y \rangle$  along with  $\theta$  versus applied current  $j$  for the  $N_{\text{sk}}/N_m = 3$  trimer lattice system from Fig. 1(b). The pinned phase I appears for  $j \leq 0.6 \times 10^{10} \text{ A m}^{-2}$ , while the transverse motion phase  $\text{II}_a$  spans the range  $0.6 \times 10^{10} \text{ A m}^{-2} < j \leq 1.4 \times 10^{10} \text{ A m}^{-2}$ . At higher drives we find phase V motion. There is also a small region around  $j = 4.2 \times 10^{10} \text{ A m}^{-2}$  where both velocities peak and strong  $45^\circ$  directional locking is present. In Fig. 3(c) we illustrate the skyrmion motion in phase  $\text{II}_a$  at  $j = 1 \times 10^{10} \text{ A m}^{-2}$ . The flow is in the form of a soliton, where a single skyrmion jumps from one well to the next and causes another skyrmion to jump to the next well. One skyrmion in each trimer does not participate in the motion, as indicated by the absence of trajectories for the skyrmions on the right side of each well. Figure 3(d) shows the motion of a single skyrmion during disordered phase V flow at  $j = 5 \times 10^{10} \text{ A m}^{-2}$ , where some pinned skyrmions are still present. The  $45^\circ$  directional locking state at  $j = 4.2 \times 10^{10} \text{ A m}^{-2}$

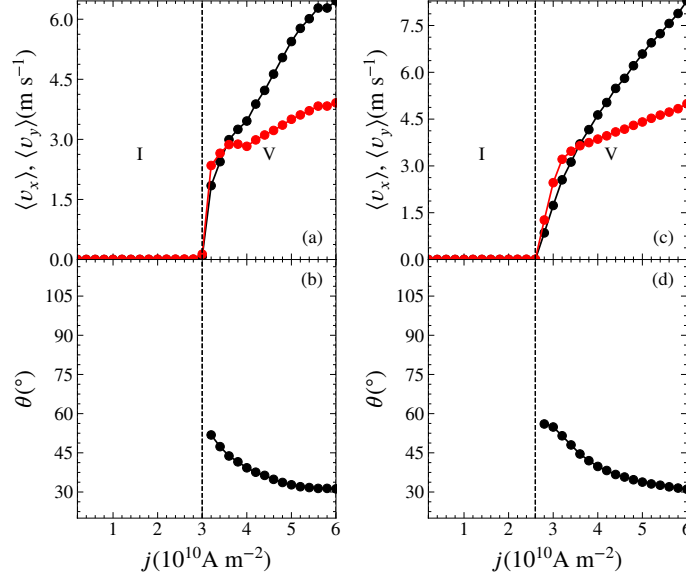


**Figure 6.** (a, c) Average skyrmion velocities  $\langle v_x \rangle$  (black) and  $\langle v_y \rangle$  (red) and (b, d) the corresponding skyrmion Hall angle  $\theta$  vs  $j$  from an atomistic model on a triangular substrate. (a, b) The  $N_{\text{sk}}/N_m = 2.0$  system from Fig. 1(e). (c, d) The  $N_{\text{sk}}/N_m = 3.0$  system from Fig. 1(f). I: pinned phase. V: disordered motion.

is plotted in Fig. 3(e), where only a single skyrmion trajectory is drawn. Instead of soliton flow, all of the skyrmions are flowing in this state. For higher drives, the flow becomes more disordered and some of the skyrmions repin, resulting in a velocity drop above the directionally locked state.

In Fig. 4(a, b) we show  $\langle v_x \rangle$ ,  $\langle v_y \rangle$ , and  $\theta_{\text{sk}}$  vs  $j$  for the system in Fig. 1(c) at the  $N_{\text{sk}}/N_m = 3/2$  filling. In this case, there is a much larger pinned phase I that persists up to  $j = 2.4 \times 10^{10} \text{ A m}^{-2}$ , followed by extended regions of flow locked along  $45^\circ$  for  $2.4 \times 10^{10} \text{ A m}^{-2} < j \leq 5.2 \times 10^{10} \text{ A m}^{-2}$ , which we label phase II<sub>b</sub>. At higher drives, the system transitions to disordered phase V flow, and a velocity drop appears at the II<sub>b</sub> to V transition. There is a well-defined step feature in  $\theta$  associated with the  $45^\circ$  locking state. In Fig. 4(c), we show the skyrmion trajectories for the phase II<sub>b</sub> flow at  $j = 3 \times 10^{10} \text{ A m}^{-2}$ . A solitonic flow passes only through the dimer wells and the motion runs along  $45^\circ$ . The sites containing only one skyrmion remain permanently pinned. Figure 4(d) shows the trajectory of a single skyrmion at  $j = 6 \times 10^{10} \text{ A m}^{-2}$  in phase V, where the motion is more disordered and there is a mixture of pinned monomers and dimers. Compared to the  $N_{\text{sk}}/N_m = 2.0$  system, the  $N_{\text{sk}}/N_m = 3/2$  does not have a regime in which the motion runs completely transverse to the applied current. Instead, the transverse flow state has been replaced by a pinned phase.

For the dimer-trimer system in Fig. 1(d) at a filling of  $N_{\text{sk}}/N_m = 5/2$ , in Fig. 5(a, b) we plot  $\langle v_x \rangle$ ,  $\langle v_y \rangle$ , and  $\theta$  versus  $j$ . The pinned region is reduced in size and appears when  $j \leq 0.4 \times 10^{10} \text{ A m}^{-2}$ , while there is a region of transverse II<sub>a</sub> flow over the range  $0.4 \times 10^{10} \text{ A m}^{-2} < j \leq 1.6 \times 10^{10} \text{ A m}^{-2}$ . As the drive increases,  $\langle v_y \rangle$  increases linearly throughout region II<sub>a</sub> and then passes through a sharp drop when the system enters the disordered flow phase V. For this filling, we do not observe any  $45^\circ$  directional locking, and  $\theta$  smoothly approaches the intrinsic value as the current increases. In

Fig. 5(c), skyrmion trajectories from the  $\text{II}_a$  phase at  $j = 1 \times 10^{10} \text{ A m}^{-2}$  indicate that the motion consists of  $y$  direction soliton flow. The trajectory of a single skyrmion in the disordered phase V flow state at  $j = 3 \times 10^{10} \text{ A m}^{-2}$  appears in Fig. 5(d).

#### 4. Dynamics of Skyrmion Molecular Crystals on Triangular Substrates

We next consider the case of driven skyrmion molecular crystals on triangular substrates. We use the same parameters as the square substrate; the only difference is the sample size, which is changed to  $L_y = 84 \text{ nm}$  and  $L_x = 96.5 \text{ nm}$ . In general, we find a strong pinning effect for triangular substrates. The flow is more disordered, and the  $90^\circ$  locking flow phases that appear on the square substrate do not occur for the triangular substrate.

In Fig. 6(a, b) we plot  $\langle v_x \rangle$ ,  $\langle v_y \rangle$ , and  $\theta$  versus  $j$  for the  $N_{\text{sk}}/N_m = 2.0$  dimer filling for skyrmions on a triangular substrate that appears in Fig. 1(e). There is an extended pinned regime that ends at  $j = 3 \times 10^{10} \text{ A m}^{-2}$  and is followed by a disordered flow state in which both  $\langle v_x \rangle$  and  $\langle v_y \rangle$  increase with increasing drive. Just above depinning,  $\theta$  takes a value slightly lower than  $60^\circ$ , corresponding to a partial locking of the skyrmion motion to the  $60^\circ$  symmetry direction of the triangular substrate. In Fig. 7(a) we show the trajectories of a single skyrmion at  $j = 3.2 \times 10^{10} \text{ A m}^{-2}$  where the flow is partially disordered and there is partial channeling along  $60^\circ$ . At  $j = 5 \times 10^{10} \text{ A m}^{-2}$ , the plot of a single skyrmion trajectory in Fig. 7(c) indicates that the motion is much more disordered compared to the phase V flow in the square substrate illustrated in 2(e), and there is some tendency for the skyrmions to move along  $60^\circ$ . As  $j$  increases, Fig. 6(b) shows that  $\theta$  gradually decreases toward the intrinsic value.

We show  $\langle v_x \rangle$ ,  $\langle v_y \rangle$ , and  $\theta$  versus  $j$  for the  $N_{\text{sk}}/N_m = 3.0$  trimer filling of a triangular substrate in Fig. 6(c, d). Similar to what we observed for the dimer state, there is no transverse motion, and the flow just above depinning initially runs along a direction close to a major substrate symmetry direction. The Hall angle is close to  $60^\circ$  above depinning and decreases toward the intrinsic value as the drive increases. In Fig. 7(b) we plot the trajectory of a single skyrmion at  $j = 3.2 \times 10^{10} \text{ A m}^{-2}$  where the flow is partially disordered and partial channeling along  $60^\circ$  is present. A single trajectory at a higher drive of  $j = 5 \times 10^{10} \text{ A m}^{-2}$ , shown in Fig. 7(d), indicates that the channeling is increasingly lost and the flow is becoming more disordered.

Figure 8(a, b) shows  $\langle v_x \rangle$ ,  $\langle v_y \rangle$ , and  $\theta$  versus  $j$  for the  $N_{\text{sk}}/N_m = 3/2$  monomer-dimer filling on the triangular substrate. For  $j > 4.6 \times 10^{10} \text{ A m}^{-2}$ , the flow locks along  $30^\circ$  and creates a step feature in  $\theta$ . We label this directionally locked state phase  $\text{II}_c$ . Between depinning and the onset of phase  $\text{II}_c$  is a transitional phase we term  $\text{III}_a$  in which soliton-like motion occurs but there is no directional locking. In Fig. 7(e), the plot of all skyrmion trajectories at  $j = 5 \times 10^{10} \text{ A m}^{-2}$  demonstrates that the  $\text{II}_c$  ordered motion is a directionally locked phase with flow occurring along  $30^\circ$ . We plot  $\langle v_x \rangle$ ,  $\langle v_y \rangle$ , and  $\theta_{\text{sk}}$  versus  $j$  for the dimer-trimer  $N_{\text{sk}}/N_m = 5/2$  filling in Fig. 8(c, d). The transport signatures have features very similar to those that appear at the dimer and trimer fillings. In Fig. 7(f) we show the trajectory of a single skyrmion at  $N_{\text{sk}}/N_m = 5/2$  for  $j = 5 \times 10^{10} \text{ A m}^{-2}$ , where the flow is disordered.

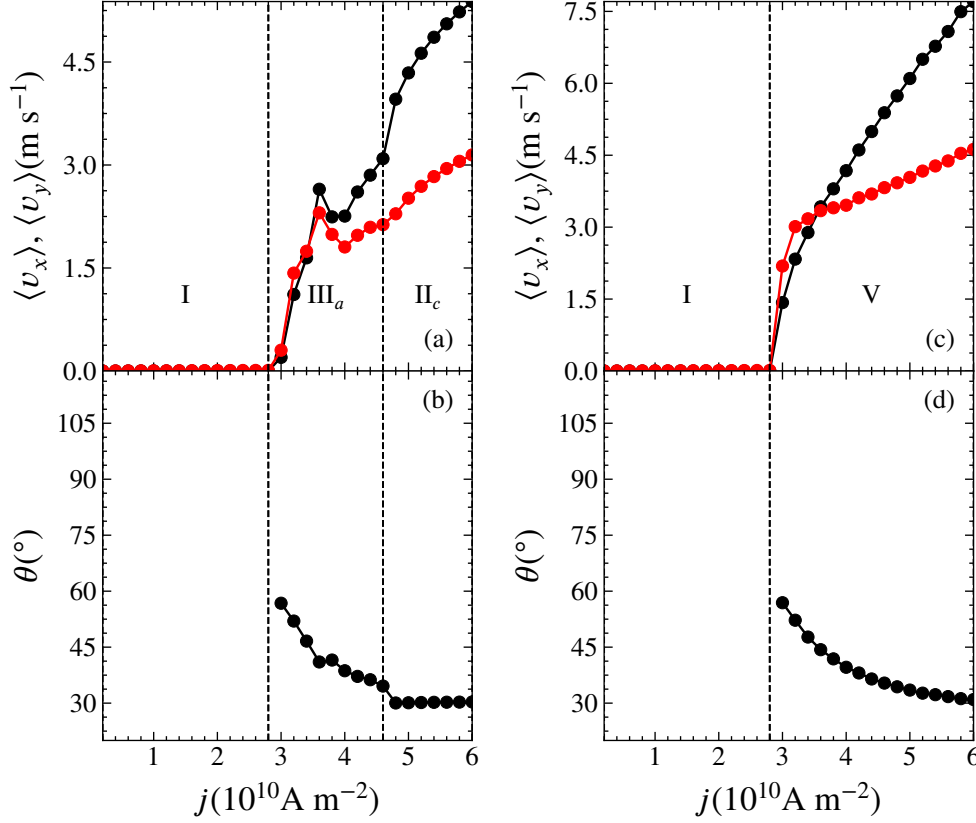


**Figure 7.** Skyrmion trajectories at representative drives for a triangular substrate with the same parameters as the square substrate in Fig. 1(a-d) from an atomistic model. (a) Trajectory of a single skyrmion for the dimer state with  $N_{\text{sk}}/N_m = 2.0$  at  $j = 3.2 \times 10^{10} \text{ A m}^{-2}$ . (b) Trajectory of a single skyrmion for the trimer state with  $N_{\text{sk}}/N_m = 3.0$  at  $j = 3.2 \times 10^{10} \text{ A m}^{-2}$ . (c) Trajectory of a single skyrmion for the dimer state with  $N_{\text{sk}}/N_m = 2.0$  at  $j = 5 \times 10^{10} \text{ A m}^{-2}$ . (d) Trajectory of a single skyrmion for the trimer state with  $N_{\text{sk}}/N_m = 3.0$  at  $j = 5 \times 10^{10} \text{ A m}^{-2}$ . (e) Trajectories of all skyrmions for the  $N_{\text{sk}}/N_m = 3/2$  monomer-dimer filling in the directional locking phase II<sub>c</sub> at  $j = 5 \times 10^{10} \text{ A m}^{-2}$  where the motion is along  $30^\circ$ . (f) Trajectory of a single skyrmion for the  $N_{\text{sk}}/N_m = 5/2$  dimer-trimer filling in the disordered flow state at  $j = 5 \times 10^{10} \text{ A m}^{-2}$ .

## 5. Particle-Based Model

We next turn to results from a particle-based model. As described in the Methods section, we match the parameters of the particle-based simulations to those of the atomistic simulations. We first focus on the  $N_{\text{sk}}/N_m = 2.0$  filling for the square substrate, which forms the dimer state shown in Fig. 1(a). In Fig. 9(a,b) we plot  $\langle V_x \rangle$ ,  $\langle V_y \rangle$ , and  $\theta$  versus  $F_D$ . A pinned phase I appears for  $F_D < 0.075$ , while we observe the  $90^\circ$  transverse motion phase II<sub>a</sub> for  $0.075 < F_D < 0.1$ . In Fig. 9(c) we show the skyrmion trajectories at  $F_D = 0.085$  in phase II<sub>a</sub>. There is occasional hopping of individual skyrmions along the  $x$  direction, but the majority of the motion is locked along the  $y$  direction. Over the range  $0.125 < F_D < 0.26$ , the  $45^\circ$  directional locking

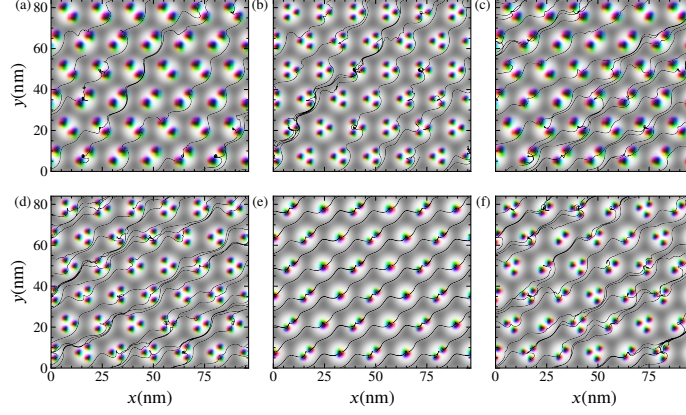


**Figure 8.** (a, c) Average skyrmion velocities  $\langle v_x \rangle$  (black) and  $\langle v_y \rangle$  (red) and (b, d) the corresponding skyrmion Hall angle  $\theta$  vs  $j$  from an atomistic model on a triangular substrate. (a, b) The  $N_{\text{sk}}/N_m = 3/2$  monomer-dimer filling from Fig. 1(g). (c, d) The  $N_{\text{sk}}/N_m = 5/2$  dimer-trimer filling from Fig. 1(h). I: pinned phase.  $\text{II}_c$ :  $30^\circ$  directional locking state.  $\text{III}_a$ : transitional soliton flow regime with no directional locking. V: disordered motion.

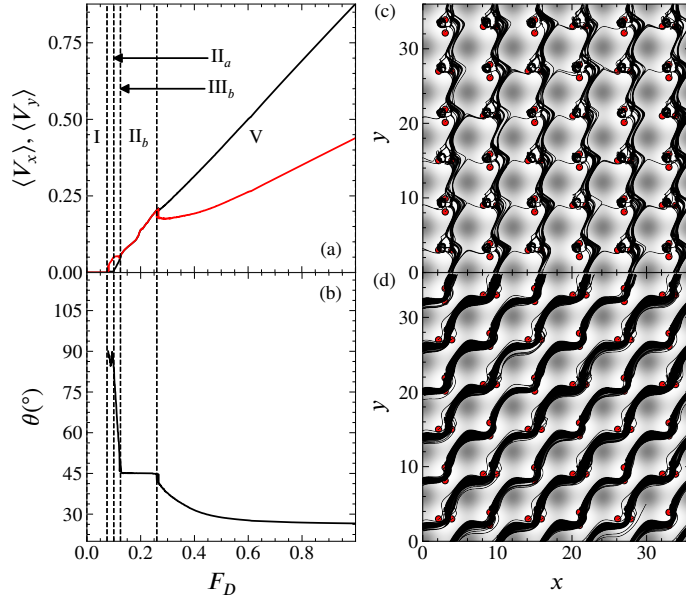


**Figure 9.** (a) Average skyrmion velocities  $\langle V_x \rangle$  (black) and  $\langle V_y \rangle$  (red) and (b) the skyrmion Hall angle  $\theta$  vs  $F_D$  from a particle-based model at a dimer filling of  $N_{\text{sk}}/N_m = 2.0$  on a square substrate. I: pinned phase.  $\text{II}_a$ :  $90^\circ$  transverse motion.  $\text{II}_b$ :  $45^\circ$  directionally locked motion.  $\text{III}_b$ : transitional regime between phases  $\text{II}_a$  and  $\text{II}_b$ . V: disordered motion. (c) Skyrmion trajectories in phase  $\text{II}_a$  at  $F_D = 0.085$ . (d) Skyrmion trajectories in phase  $\text{II}_b$  at  $F_D = 0.19$ . Animations showing the phase  $\text{II}_a$  and  $\text{II}_b$  motion are available in the supplemental material [62].

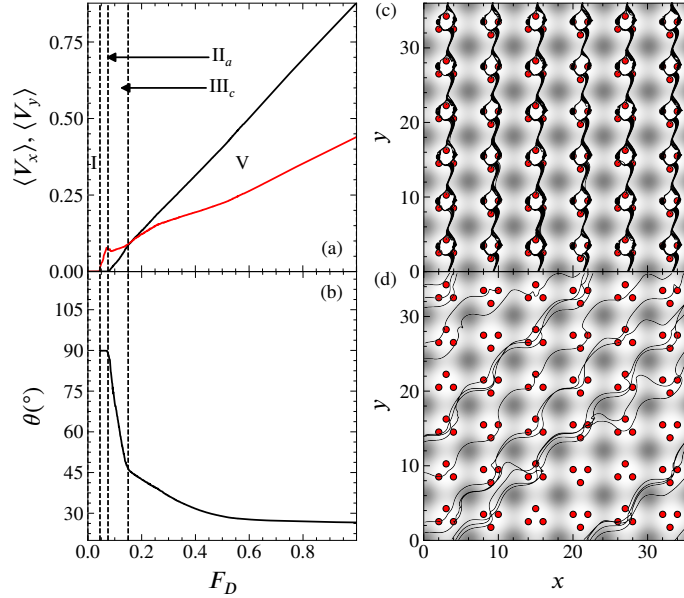


**Figure 10.** Average skyrmion velocities  $\langle V_x \rangle$  (black) and  $\langle V_y \rangle$  (red) and (b) the skyrmion Hall angle  $\theta$  vs  $F_D$  from a particle-based model at a trimer filling of  $N_{\text{sk}}/N_m = 3.0$  on a square substrate. I: pinned phase. II<sub>a</sub>: 90° transverse motion. III<sub>c</sub>: transitional regime between phases II<sub>a</sub> and V. V: disordered motion. (c) Skyrmion trajectories in phase II<sub>a</sub> at  $F_D = 0.05$ . II<sub>a</sub>. (d) Trajectory of a single skyrmion in phase V at  $F_D = 0.2$ . Animations showing the phase II<sub>a</sub> and V motion are available in the supplemental material [62].

phase II<sub>b</sub> appears. The motion is solitonic, as shown Fig. 9(d) at  $F_D = 0.19$ . In between phases II<sub>a</sub> and II<sub>b</sub>, over the range  $0.1 < F_D < 0.125$ , there is a transitional state labeled III<sub>b</sub> in which there is a combination of transverse motion with an increased amount of hopping along the  $x$  direction. At higher drives of  $F_D > 0.26$ , the system enters the more disordered phase V, there is no directional locking, and the skyrmion Hall angle approaches the intrinsic value. A drop in  $\langle V_y \rangle$  corresponding to negative differential conductivity occurs at the transition between phase II<sub>b</sub> and phase V.

In Fig. 10(a) we plot  $\langle V_x \rangle$ ,  $\langle V_y \rangle$ , and  $\theta$  versus  $F_D$  for the trimer state at  $N_{\text{sk}}/N_m = 3.0$  on a square substrate. The pinned phase I depins into the transverse motion phase II<sub>a</sub>. We illustrate the skyrmion trajectories in phase II<sub>a</sub> at  $F_D = 0.05$  in Fig. 10(c), which shows that the transverse flow occurs via the motion of a soliton. As the drive increases we observe a transitional state, labeled III<sub>c</sub>, between phase II<sub>a</sub> and the disordered phase V flow that appears at higher drives. Unlike the dimer lattice state, we observe no phase II<sub>b</sub> or 45° directionally locked flow. This is due to the creation of disordered flow structures that make the motion more thermal in character and prevent ordered channels from forming along the 45° direction. For increasing drive in phase V, the motion gradually rotates into the direction of the intrinsic Hall angle. In the particle-based model, all of the skyrmions within each trimer participate in the phase II<sub>a</sub> motion. This is in contrast to the atomistic model results from Fig. 3(c), where one skyrmion in each trimer remained stationary throughout the phase II<sub>a</sub> regime. The difference arises because the individual skyrmions can distort

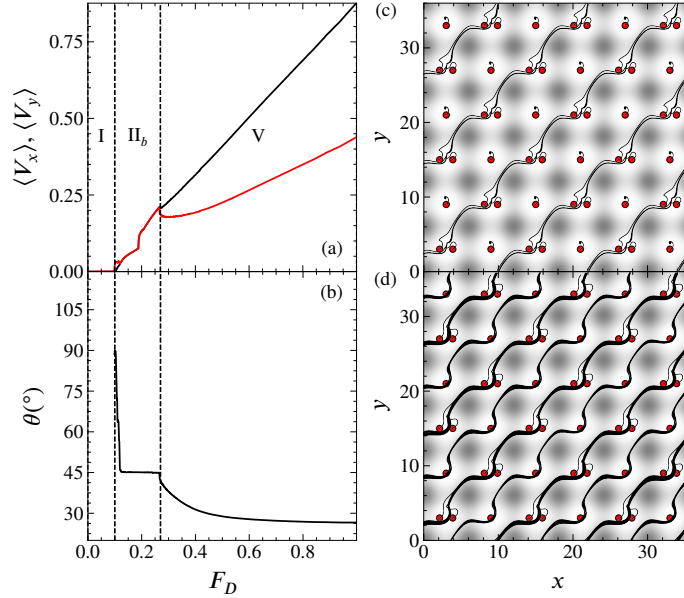


**Figure 11.** (a) Average skyrmion velocities  $\langle V_x \rangle$  (black) and  $\langle V_y \rangle$  (red) and (b) the skyrmion Hall angle  $\theta$  vs  $F_D$  from a particle-based model at a monomer-dimer filling of  $N_{\text{sk}}/N_m = 3/2$  on a square substrate. I: pinned phase. II<sub>b</sub>: 45° directionally locked motion. V: disordered motion. (c) Skyrmion trajectories in phase II<sub>b</sub> at  $F_D = 0.15$ . (d) Trajectory of a single skyrmion in phase II<sub>b</sub> at  $F_D = 0.2$  where all of the skyrmions are moving. Animations showing the phase II<sub>b</sub> motion at different  $F_D$  values are available in the supplemental material [62].

in the atomistic model but have fixed effective sizes in the particle-based model.

We plot  $\langle V_x \rangle$ ,  $\langle V_y \rangle$ , and  $\theta$  versus  $F_D$  in Fig. 11(a, b) for a monomer-dimer filling of  $N_{\text{sk}}/N_m = 3/2$  on a square substrate. A pinned phase I appears for  $F_D < 0.1$ , and there is a 45° directional locking phase II<sub>b</sub> over the region  $0.1 < F_D < 0.27$ . The directionally locked phase II<sub>b</sub> contains an internal depinning transition. For lower drives, soliton motion occurs only along diagonal channels that contain dimers, while channels containing monomers remain pinned, as illustrated in Fig. 11(c) at  $F_D = 0.15$ . For higher drives, the monomers can also participate in the soliton motion, as shown in Fig. 11(d) at  $F_D = 0.2$ . At the transition from phase II<sub>b</sub> to the high drive disordered phase V flow, there is a drop in the skyrmion velocity.

For the dimer-trimer filling of the square substrate at  $N_{\text{sk}}/N_m = 5/2$ , Fig. 12(a, b) shows  $\langle V_x \rangle$ ,  $\langle V_y \rangle$ , and  $\theta_{\text{sk}}$  versus  $F_D$ , where phases I, II<sub>a</sub>, III<sub>b</sub>, II<sub>b</sub>, and V appear. The transverse motion in phase II<sub>a</sub> occurs through soliton flow, as shown in Fig. 12(c) at  $F_D = 0.05$ . In the directionally locked phase II<sub>b</sub>, the skyrmions move preferentially along a 45° path with some occasional hopping along the  $x$  direction, as illustrated in Fig. 12(d) at  $F_D = 0.2$ .

Figure 13(a, b) shows  $\langle V_x \rangle$ ,  $\langle V_y \rangle$ , and  $\theta$  versus  $F_D$  for the dimer filling of  $N_{\text{sk}}/N_m = 2.0$  on a triangular substrate. From the pinned phase I, no transverse motion occurs at depinning, and the initial flow is of solitons moving along 60°, labeled phase II<sub>d</sub>. This phase II<sub>d</sub> is very narrow and although it also exists in Fig. 13(a), it is only highlighted in Fig. 13(b). As  $F_D$  increases, we find region III<sub>d</sub> flow, which is transitional between regions II<sub>d</sub> and II<sub>c</sub>. In region III<sub>d</sub>, illustrated in Fig. 13(c) at



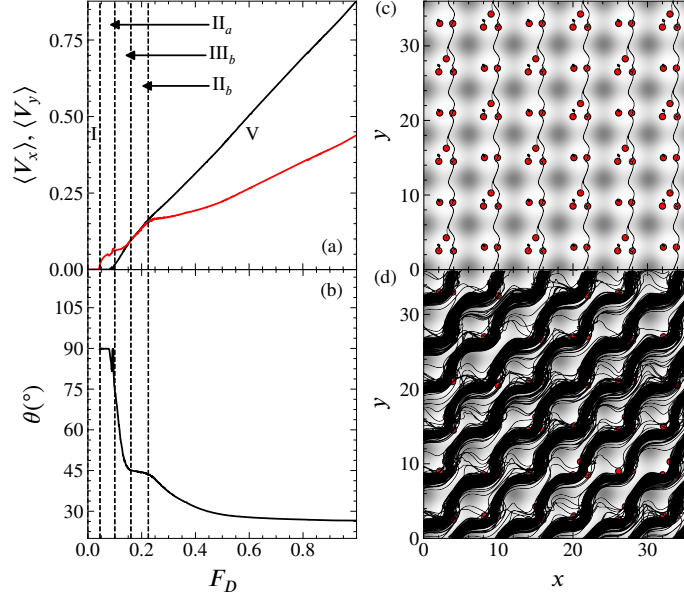


**Figure 12.** (a) Average skyrmion velocities  $\langle V_x \rangle$  (black) and  $\langle V_y \rangle$  (red) and (b) the skyrmion Hall angle  $\theta$  vs  $F_D$  from a particle-based model at a dimer-trimer filling of  $N_{\text{sk}}/N_m = 5/2$  on a square substrate. I: pinned phase. II<sub>a</sub>: 90° transverse motion. II<sub>b</sub>: 45° directionally locked motion. III<sub>b</sub>: transitional regime between phases II<sub>a</sub> and II<sub>b</sub>. V: disordered motion. (c) Skyrmion trajectories in phase II<sub>a</sub> at  $F_D = 0.05$ . (d) Trajectory of a single skyrmion in phase II<sub>b</sub> at  $F_D = 0.2$ . Animations showing the phase II<sub>a</sub> and II<sub>b</sub> motion are available in the supplemental material [62].

$F_D = 0.35$ ,  $\theta$  decreases with increasing  $F_D$  until there is a directional locking along 30° and the system enters phase II<sub>c</sub>. A small dip in the velocities appears at the transition between phases III<sub>d</sub> and II<sub>c</sub>. The velocities increase linearly with increasing drive in phase II<sub>c</sub> and the flow is ordered, as shown in Fig. 13(d) at  $F_D = 0.5$ . At higher drives, the system transitions to phase V, where there is no directional locking and the flow is disordered.

In Fig. 14(a, b) we plot  $\langle V_x \rangle$ ,  $\langle V_y \rangle$ , and  $\theta$  versus  $F_D$  for a trimer filling of  $N_{\text{sk}}/N_m = 3.0$  on a triangular substrate. We again observe phases I, II<sub>d</sub>, III<sub>d</sub>, II<sub>c</sub>, and V, and find no transverse 90° motion. When the system depins into the locked phase II<sub>d</sub> flow, highlighted in Fig. 14(b) at  $F_D = 0.14$ ,  $\theta = 60^\circ$  and the motion is almost entirely along the major symmetry direction of the substrate, with occasional hopping in the  $x$  direction. As  $F_D$  increases, the system enters the transitional region III<sub>d</sub> and the skyrmion Hall angle  $\theta$  decreases until it becomes locked to 30° at the transition into phase II<sub>c</sub>. The trajectories at  $F_D = 0.5$ , illustrated in Fig. 14(d), fall in the center of the phase II<sub>c</sub> range which extends from  $0.4 < F_D < 0.6$ , and show channels of motion along 30° with occasional hopping between adjacent wells. At high drives in phase V, the flow is disordered.

The monomer-dimer filling of  $N_{\text{sk}}/N_m = 3/2$  for a triangular substrate is shown in Fig. 15(a, b), where we plot  $\langle V_x \rangle$ ,  $\langle V_y \rangle$ , and  $\theta_{\text{sk}}$  versus  $F_D$ . The phases that appear are similar to those found for the  $N_{\text{sk}}/N_m = 2.0$  dimer filling, and there is a strong drop in the velocity at the III<sub>d</sub> to II<sub>c</sub> transition. Fig. 15(c) shows the trajectory

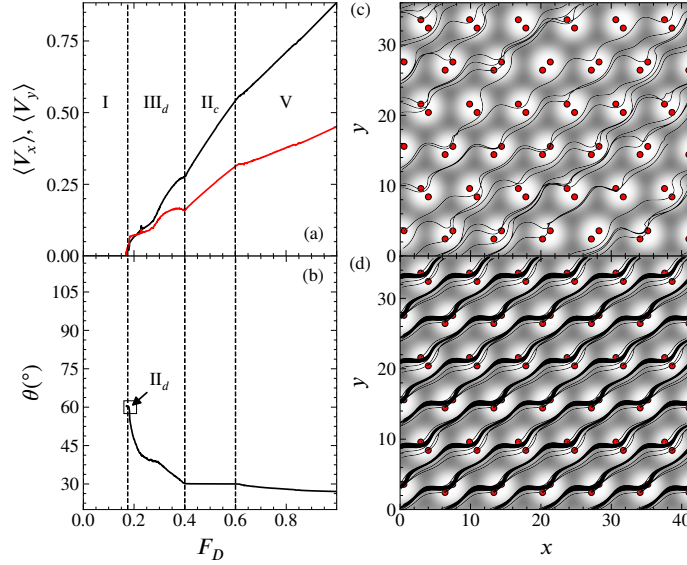


**Figure 13.** (a) Average skyrmion velocities  $\langle V_x \rangle$  (black) and  $\langle V_y \rangle$  (red) and (b) the skyrmion Hall angle  $\theta$  vs  $F_D$  from a particle-based model at a dimer filling of  $N_{\text{sk}}/N_m = 2.0$  on a triangular substrate. I: pinned phase.  $II_c$ : 30° directionally locked motion.  $II_d$ : 60° directionally locked motion.  $III_d$ : transitional regime between phases  $II_d$  and  $II_c$ . V: disordered motion. (c) Trajectory of a single skyrmion in phase  $III_d$  at  $F_D = 0.35$ . (d) Skyrmion trajectories in phase  $II_c$  at  $F_D = 0.5$ . Animations showing the phase  $III_d$  and  $II_c$  motion are available in the supplemental material [62].

of a single skyrmion in phase  $III_d$  at  $F_D = 0.3$ , where the motion is not locked to the substrate but smoothly changes in angle as the drive increases. In Fig. 15(d) we show trajectories for all of the skyrmions in phase  $II_c$  at  $F_D = 0.5$ , where the motion is almost entirely locked along 30° with occasional hops in the  $x$  direction. The directional locking is not quite as strong as what we observe for the atomistic model in Fig. 8(e), where no  $x$  direction hopping occurs, and this is due to the inability of the particle-based skyrmions to deform.

In Fig. 16(a, b) we plot  $\langle V_x \rangle$ ,  $\langle V_y \rangle$ , and  $\theta_{\text{sk}}$  versus  $F_D$  for a triangular substrate at the dimer-trimer filling of  $N_{\text{sk}}/N_m = 5/2$ . The directionally locked phase  $II_d$ , in which the skyrmions move along 60°, that appears just above depinning is much more extended compared to the fillings that have been described above, and is illustrated at  $F_D = 0.15$  in Fig. 16(c). After the system passes through a transitional  $III_d$  state, a 30° directionally locked phase  $II_c$  appears which has the motion shown for a drive of  $F_D = 0.5$  in Fig. 16(d). At higher drives, the system enters the disordered flow region V state.

In general, the particle model qualitatively shows the same phases as the atomistic models, including transverse motion, soliton flows, directional locking, and the disordered phases; however, there are several quantitative differences between the two models. This could be due to the ability of the skyrmions to distort or change size as they move, which is present in the atomistic model but not in the particle-based model. These distortions and size changes introduce additional fluctuations so that the robustness of directional locking to the higher order symmetry locking directions

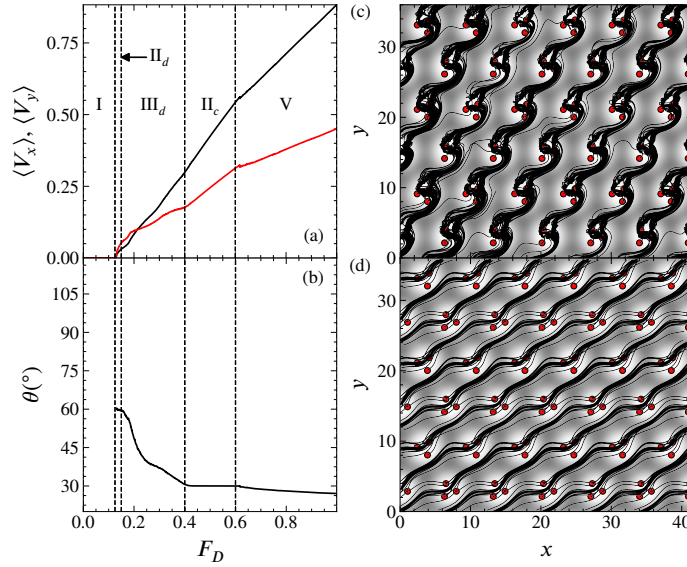


**Figure 14.** (a) Average skyrmion velocities  $\langle V_x \rangle$  (black) and  $\langle V_y \rangle$  (red) and (b) the skyrmion Hall angle  $\theta$  vs  $F_D$  from a particle-based model at a trimer filling of  $N_{\text{sk}}/N_m = 3.0$  on a triangular substrate. I: pinned phase.  $II_d$ : 60° directionally locked motion.  $II_c$ : 30° directionally locked motion.  $III_d$ : transitional regime between phases  $II_d$  and  $II_c$ . V: disordered motion. (c) Skyrmion trajectories in phase  $II_d$  at  $F_D = 0.14$ . (d) Trajectory of a single skyrmion in phase  $II_c$  at  $F_D = 0.5$ . Animations showing the phase  $II_d$  and  $II_c$  motion are available in the supplemental material [62].

is reduced. For both models, we find strong solitonic motion in the mixed molecular crystal states, when a portion of the skyrmions are pinned and kink motion can occur. This is due to the strong difference in the effectiveness of the pinning for monomers compared to dimers. Since the monomers can sit at the bottom of the pinning well, they are much more difficult to depin than individual skyrmions of a dimer.

## 6. Varied Anisotropy

We next consider the evolution of the phases over a range of anisotropies to show that the results are robust for the atomistic model. In Fig. 17(a, b), we plot heat maps of the net skyrmion velocity  $\langle v \rangle$  and the Hall angle  $\theta$  as a function of  $K_0/J$  versus  $j$  for a square substrate at the dimer filling of  $N_{\text{sk}}/N_m = 2.0$ . For  $K_0/J > 0.15$ , there is a region of transverse motion where the Hall angle is nearly 90°. The pinned region with  $\langle v \rangle = 0$  and the transverse flow region with  $\theta = 90^\circ$  both grow in extent as  $K_0/J$  increases. This indicates that a critical level of anisotropy is required to permit transverse motion to occur. Figure 17(c, d) shows  $\langle v \rangle$  and  $\theta$  heat maps for the same system at a trimer filling of  $N_{\text{sk}}/N_m = 3.0$ . The overall trend of the phases is similar to the dimer filling, and transverse motion only occurs when  $K_0/J > 0.15$ . The trimer filling in Fig. 17(c) exhibits some instances of negative differential mobility, where the velocity is greatest at intermediate drives.

In Fig. 18(a, b), we show heat maps of  $\langle v \rangle$  and  $\theta$  as a function of  $K_0/J$  versus  $j$  for a square substrate at the monomer-dimer filling of  $N_{\text{sk}}/N_m = 3/2$ . Here, the pinned

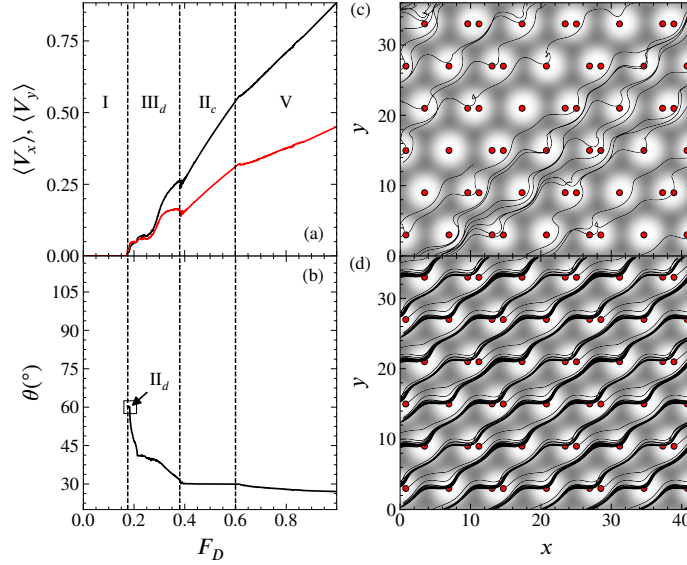


**Figure 15.** (a) Average skyrmion velocities  $\langle V_x \rangle$  (black) and  $\langle V_y \rangle$  (red) and (b) the skyrmion Hall angle  $\theta$  vs  $F_D$  from a particle-based model at a monomer-dimer filling of  $N_{\text{sk}}/N_m = 3/2$  on a triangular substrate. I: pinned phase. II<sub>d</sub>: 60° directionally locked motion. II<sub>c</sub>: 30° directionally locked motion. III<sub>d</sub>: transitional regime between phases II<sub>d</sub> and II<sub>c</sub>. V: disordered motion. (c) Trajectory of a single skyrmion in phase III<sub>d</sub> at  $F_D = 0.3$ . (d) Skyrmion trajectories in phase II<sub>c</sub> at  $F_D = 0.5$ . Animations showing the phase III<sub>d</sub> and II<sub>c</sub> motion are available in the supplemental material [62].

region is very large and extends up to  $j = 3.2 \times 10^{10} \text{ A m}^{-2}$ . Additionally, there is no transverse motion regime, and the Hall angle remains close to  $\theta = 30^\circ$  for all moving states. The extended pinned regime arises because the monomers are much more strongly pinned than the dimers. Since the skyrmions have a checkerboard ordering at this filling, when dimers attempt to depin by moving in the transverse direction, they are blocked by the more strongly pinned monomers. The  $\langle v \rangle$  and  $\theta$  heat maps as a function of  $K_0/J$  versus  $j$  shown in Fig. 18(c, d) for the dimer-trimer filling of  $N_{\text{sk}}/N_m = 5/2$  indicate that the pinned regime has become much smaller, and a regime of transverse motion emerges when  $K_0/J > 0.16$ .

For atomistic simulations of the triangular substrate, in Fig. 19(a, b) we plot heat maps of  $\langle v \rangle$  and  $\theta$  as a function of  $K_0/J$  versus  $j$  at the dimer filling of  $N_{\text{sk}}/N_m = 2.0$ . The pinned region is much larger than for the dimer state on a square substrate, and increases linearly in width with increasing  $K_0/J$ . The enhanced pinning arises because the drive is not aligned with one of the major symmetry directions of the triangular substrate, such as  $60^\circ$ , whereas for the square substrate, both the current and the drive are aligned with major symmetry directions of  $90^\circ$  and  $0^\circ$ . When depinning occurs on the triangular substrate, the Hall angle is close to  $60^\circ$ , and  $\theta$  decreases toward the intrinsic Hall angle value as  $j$  increases. There are several windows of directional locking to  $30^\circ$ , which appear as non-monotonic changes in velocity and a plateau of the Hall angle at  $30^\circ$ . For the trimer filling of  $N_{\text{sk}}/N_m = 3.0$  on the triangular lattice, the heat maps of  $\langle v \rangle$  and  $\theta$  as a function of  $K_0/J$  versus  $j$  in Fig. 19(c, d) indicate that there is again a strong pinning regime that increases in width with increasing  $K_0/J$ ,

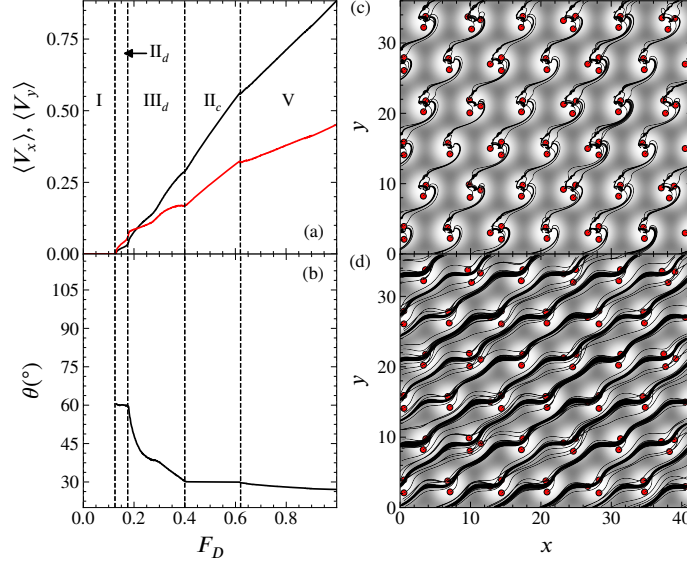


**Figure 16.** (a) Average skyrmion velocities  $\langle V_x \rangle$  (black) and  $\langle V_y \rangle$  (red) and (b) the skyrmion Hall angle  $\theta$  vs  $F_D$  from a particle-based model at a dimer-trimer filling of  $N_{\text{sk}}/N_m = 5/2$  on a triangular substrate. I: pinned phase.  $II_d$ :  $60^\circ$  directionally locked motion.  $II_c$ :  $30^\circ$  directionally locked motion.  $III_d$ : transitional regime between phases  $II_d$  and  $II_c$ . V: disordered motion. (c) Skyrmion trajectories in phase  $II_d$  at  $F_D = 0.15$ . (d) Skyrmion trajectories in phase  $II_c$  at  $F_D = 0.5$ . Animations showing the phase  $II_d$  and  $II_c$  motion are available in the supplemental material [62].

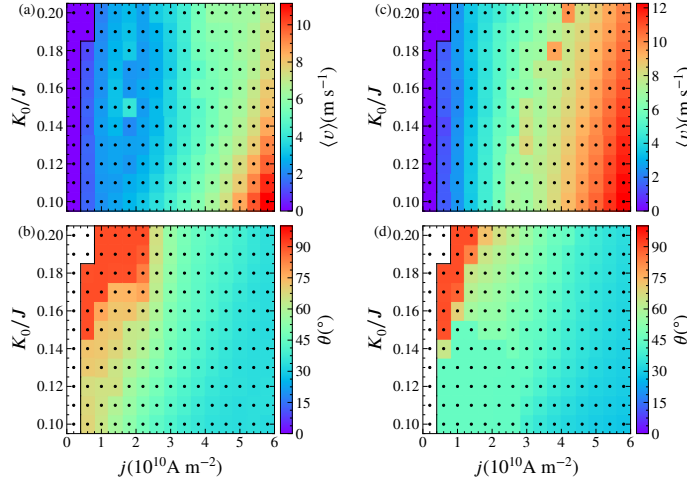


**Figure 17.** Heat maps as a function of  $K_0/J$  vs  $j$  for atomistic simulations on a square substrate. (a, c) The absolute skyrmion velocity  $\langle v \rangle = \sqrt{\langle v_x \rangle^2 + \langle v_y \rangle^2}$ . (b, d) The Hall angle  $\theta$ . (a, b) The dimer filling at  $N_{\text{sk}}/N_m = 2.0$ . (c, d) The trimer filling at  $N_{\text{sk}}/N_m = 3.0$ . For each filling, there is a critical anisotropy level  $K_0/J$  that must be exceeded for transverse motion to occur.

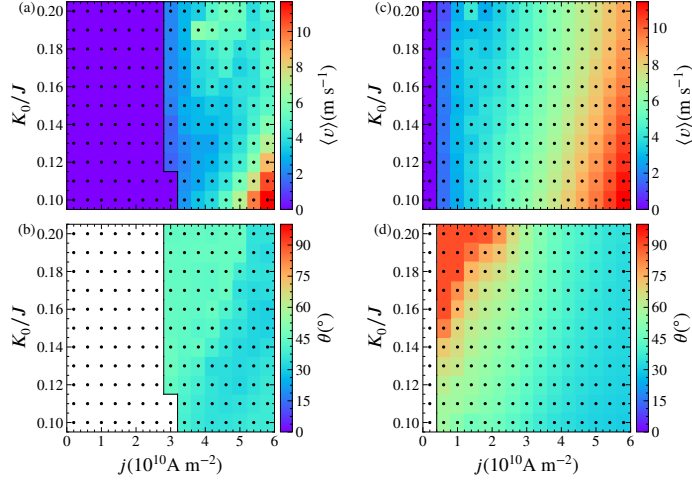


**Figure 18.** Heat maps as a function of  $K_0/J$  vs  $j$  for atomistic simulations on a square substrate. (a, c) The absolute skyrmion velocity  $\langle v \rangle = \sqrt{\langle v_x \rangle^2 + \langle v_y \rangle^2}$ . (b, d) The Hall angle  $\theta$ . (a, b) The monomer-dimer filling at  $N_{\text{sk}}/N_m = 3/2$ , where there is an extensive pinned region and no transverse motion regime. (c, d) The dimer-trimer filling at  $N_{\text{sk}}/N_m = 5/2$ . For each filling, there is a critical anisotropy level  $K_0/J$  that must be exceeded for transverse motion to occur.

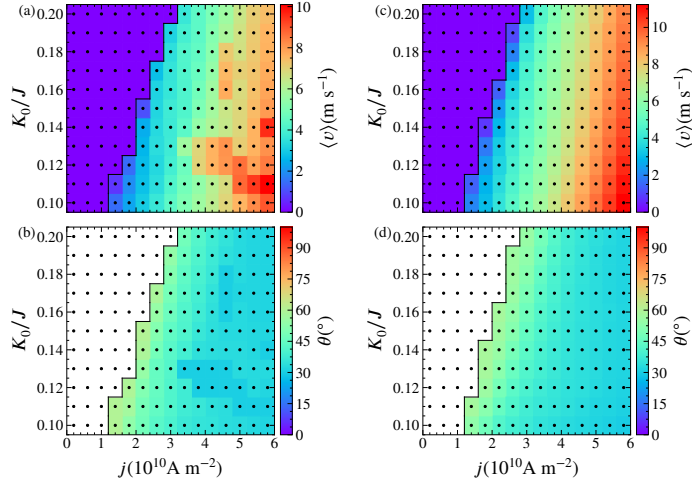


**Figure 19.** Heat maps as a function of  $K_0/J$  vs  $j$  for atomistic simulations on a triangular substrate. (a, c) The absolute skyrmion velocity  $\langle v \rangle = \sqrt{\langle v_x \rangle^2 + \langle v_y \rangle^2}$ . (b, d) The Hall angle  $\theta$ . (a, b) The dimer filling at  $N_{\text{sk}}/N_m = 2.0$ . (c, d) The trimer filling at  $N_{\text{sk}}/N_m = 3.0$ . Unlike the case of dimers and trimers on a square substrate, for the triangular substrate no transverse motion regime appears.

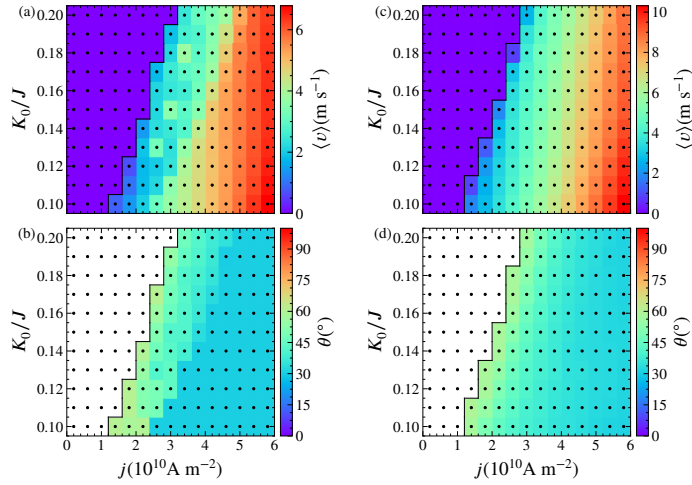


**Figure 20.** Heat maps as a function of  $K_0/J$  vs  $j$  for atomistic simulations on a triangular substrate. (a, c) The absolute skyrmion velocity  $\langle v \rangle = \sqrt{\langle v_x \rangle^2 + \langle v_y \rangle^2}$ . (b, d) The Hall angle  $\theta$ . (a, b) The monomer-dimer filling at  $N_{\text{sk}}/N_m = 3/2$ . (c, d) The dimer-trimer filling at  $N_{\text{sk}}/N_m = 5/2$ .

and the Hall angle near depinning is close to  $60^\circ$ . The trimer filling shows a smoother decrease in the Hall angle with increasing drive compared to the dimer filling.

In Fig. 20(a, b), we plot heat maps of  $\langle v \rangle$  and  $\theta$  as a function of  $K_0/J$  versus  $j$  for atomistic simulations of a triangular substrate at the monomer-dimer filling of  $N_{\text{sk}}/N_m = 3/2$ . Here an extended pinning phase is present due to the strongly pinned monomers. The heat maps of  $\langle v \rangle$  and  $\theta$  as a function of  $K_0/J$  versus  $j$  for the dimer-trimer filling of  $N_{\text{sk}}/N_m = 5/2$  in the same sample shown in Fig. 20(c, d) indicate that the Hall angle is close to  $60^\circ$  above depinning and decreases with increasing drive to the intrinsic value. The heat maps for both the square and triangular substrates for varied anisotropy  $K_0/J$  indicate that the results described in this work should remain robust over a wide range of parameters.

## 7. Summary

We have investigated the driven dynamics of skyrmion molecular crystals using atomistic and particle-based simulations of square and triangular substrates at fillings of  $N_{\text{sk}}/N_m = 3/2, 2.0, 5/2,$  and  $3.0$ , where the skyrmions form dimers, trimers, or mixed lattices that have both positional and orientational order. For a square substrate, for several of the fillings the skyrmion depinning occurs via the formation of running solitons that travel transverse to the applied current. At higher drives, the skyrmion Hall angle gradually approaches its intrinsic value and can pass through multiple steps and phases, with negative differential conductivity appearing at some of the transitions between flow states. For the square substrate, directional locking in which the motion of the skyrmions remains fixed to a constant direction over a window of applied drives can occur along  $45^\circ$ . At the monomer-dimer filling of  $N_{\text{sk}}/N_m = 3/2$ , we observe a two-step depinning process in which the dimers depin first and the monomers depin only at higher drives. Due to the blocking of the flow by

the monomers, there is no region of transverse flow above the first depinning transition. Triangular substrates do not support transverse flow due to their symmetry, but can show directional locking of the motion along  $60^\circ$  and  $30^\circ$ . Within a directionally locked state, the flow is generally well ordered. The pinned regime for the triangular substrate tends to be considerably larger than that of the square substrate because the drive is only aligned with a square substrate symmetry direction and is not aligned with a triangular substrate symmetry direction. The particle-based model produces the same qualitative phases as the atomistic model but shows several quantitative differences. We demonstrate that the phases we observe remain robust over a range of anisotropy values, and that a critical minimum anisotropy level is required in order to permit directional locking and transverse flow phases to occur.

### Acknowledgments

These resources were funded by the Fundação de Amparo à Pesquisa do Estado de São Paulo - FAPESP (Grant: 2021/04655-8). This work was supported by the US Department of Energy through the Los Alamos National Laboratory. Los Alamos National Laboratory is operated by Triad National Security, LLC, for the National Nuclear Security Administration of the U. S. Department of Energy (Contract No. 892333218NCA000001). J.C.B.S and N.P.V. acknowledge funding from Fundação de Amparo à Pesquisa do Estado de São Paulo - FAPESP (Grants J.C.B.S 2023/17545-1 and 2022/14053-8, N.P.V 2024/13248-5). We would like to thank FAPESP for providing the computational resources used in this work (Grant: 2024/02941-1).

- [1] P. Bak. Commensurate phases, incommensurate phases and the devil's staircase. *Rep. Prog. Phys.*, 45(6):587–629, 1982.
- [2] S. N. Coppersmith, D. S. Fisher, B. I. Halperin, P. A. Lee, and W. F. Brinkman. Dislocations and the commensurate-incommensurate transition in two dimensions. *Phys. Rev. B*, 25:349–363, 1982.
- [3] K. Harada, O. Kamimura, H. Kasai, T. Matsuda, A. Tonomura, and V. V. Moshchalkov. Direct observation of vortex dynamics in superconducting films with regular arrays of defects. *Science*, 274(5290):1167–1170, 1996.
- [4] T. Bohlein, J. Mikhael, and C. Bechinger. Observation of kinks and antikinks in colloidal monolayers driven across ordered surfaces. *Nature Mater.*, 11(2):126–130, 2012.
- [5] C. Reichhardt and C. J. Olson Reichhardt. Depinning and nonequilibrium dynamic phases of particle assemblies driven over random and ordered substrates: a review. *Rep. Prog. Phys.*, 80(2):026501, 2017.
- [6] H. D. Hallen, R. Seshadri, A. M. Chang, R. E. Miller, L. N. Pfeiffer, K. W. West, C. A. Murray, and H. F. Hess. Direct spatial imaging of vortices in a superconducting wire network. *Phys. Rev. Lett.*, 71:3007–3010, 1993.
- [7] C. Reichhardt and N. Grønbech-Jensen. Critical currents and vortex states at fractional matching fields in superconductors with periodic pinning. *Phys. Rev. B*, 63:054510, 2001.
- [8] S. B. Field, S. S. James, J. Barentine, V. Metlushko, G. Crabtree, H. Shtrikman, B. Ilic, and S. R. J. Brueck. Vortex configurations, matching, and domain structure in large arrays of artificial pinning centers. *Phys. Rev. Lett.*, 88:067003, 2002.
- [9] A. N. Grigorenko, S. J. Bending, M. J. Van Bael, M. Lange, V. V. Moshchalkov, H. Fangohr, and P. A. J. de Groot. Symmetry locking and commensurate vortex domain formation in periodic pinning arrays. *Phys. Rev. Lett.*, 90:237001, 2003.
- [10] M. Baert, V. V. Metlushko, R. Jonckheere, V. V. Moshchalkov, and Y. Bruynseraede. Composite flux-line lattices stabilized in superconducting films by a regular array of artificial defects. *Phys. Rev. Lett.*, 74:3269–3272, 1995.
- [11] S. Tung, V. Schweikhard, and E. A. Cornell. Observation of vortex pinning in Bose-Einstein condensates. *Phys. Rev. Lett.*, 97:240402, 2006.
- [12] M. Brunner and C. Bechinger. Phase behavior of colloidal molecular crystals on triangular light lattices. *Phys. Rev. Lett.*, 88:248302, 2002.
- [13] P. Tierno, T. H. Johansen, and T. M. Fischer. Localized and delocalized motion of colloidal particles on a magnetic bubble lattice. *Phys. Rev. Lett.*, 99:038303, 2007.



- [14] J. Mikhael, J. Roth, L. Helden, and C. Bechinger. Archimedean-like tiling on decagonal quasicrystalline surfaces. *Nature (London)*, 454(7203):501–504, 2008.
- [15] W. Zhu, C. Reichhardt, C. J. O. Reichhardt, and Y. Feng. Directional locking in a two-dimensional Yukawa solid modulated by a two-dimensional periodic substrate. *Phys. Rev. E*, 106:015202, 2022.
- [16] A. Duzgun, C. Nisoli, C. J. O. Reichhardt, and C. Reichhardt. Commensurate states and pattern switching via liquid crystal skyrmions trapped in a square lattice. *Soft Matter*, 16(13):3338–3343, 2020.
- [17] Y. Xu, S. Liu, D. A. Rhodes, K. Watanabe, T. Taniguchi, J. Hone, V. Elser, K. F. Mak, and J. Shan. Correlated insulating states at fractional fillings of moiré superlattices. *Nature (London)*, 587:214–218, 2020.
- [18] C. Reichhardt and C. J. O. Reichhardt. Depinning, melting, and sliding of generalized Wigner crystals in moiré systems. *Phys. Rev. Res.*, 7:013155, 2025.
- [19] C. Reichhardt and C. J. Olson. Novel colloidal crystalline states on two-dimensional periodic substrates. *Phys. Rev. Lett.*, 88:248301, 2002.
- [20] R. Agra, F. van Wijland, and E. Trizac. Theory of orientational ordering in colloidal molecular crystals. *Phys. Rev. Lett.*, 93:018304, 2004.
- [21] A. Šarlah, T. Franosch, and E. Frey. Melting of colloidal molecular crystals on triangular lattices. *Phys. Rev. Lett.*, 95:088302, 2005.
- [22] C. Reichhardt and C. J. Olson Reichhardt. Ordering and melting in colloidal molecular crystal mixtures. *Phys. Rev. E*, 71:062403, 2005.
- [23] A. Šarlah, E. Frey, and T. Franosch. Spin models for orientational ordering of colloidal molecular crystals. *Phys. Rev. E*, 75:021402, 2007.
- [24] C. Reichhardt and C. J. Olson Reichhardt. Vortex molecular crystal and vortex plastic crystal states in honeycomb and kagomé pinning arrays. *Phys. Rev. B*, 76:064523, 2007.
- [25] J. S. Neal, M. V. Milošević, S. J. Bending, A. Potenza, L. San Emeterio, and C. H. Marrows. Competing symmetries and broken bonds in superconducting vortex-antivortex molecular crystals. *Phys. Rev. Lett.*, 99:127001, 2007.
- [26] M. Mikulis, C. J. O. Reichhardt, C. Reichhardt, R. T. Scalettar, and G. T. Zimanyi. Re-entrant disordering of colloidal molecular crystals on two-dimensional periodic substrates. *J. Phys.: Condens. Matter*, 16(45):7909–7916, 2004.
- [27] H. Li, Z. Xiang, E. Regan, W. Zhao, R. Sailus, R. Banerjee, T. Taniguchi, K. Watanabe, S. Tongay, A. Zettl, M. F. Crommie, and F. Wang. Mapping charge excitations in generalized Wigner crystals. *Nature Nanotechnol.*, 19:618–623, 2024.
- [28] J. C. Bellizotti Souza, N. P. Vizirim, C. J. O. Reichhardt, C. Reichhardt, and P. A. Venegas. Skyrmion molecular crystals and superlattices on triangular substrates. *Phys. Rev. B*, 111:054402, 2025.
- [29] K. Hejazi, Z.-X. Luo, and L. Balents. Heterobilayer moiré magnets: Moiré skyrmions and commensurate-incommensurate transitions. *Phys. Rev. B*, 104:L100406, 2021.
- [30] R. Juge, K. Bairagi, K. G. Rana, J. Vogel, M. Sall, D. Mailly, V. T. Pham, Q. Zhang, N. Sisodia, M. Foerster, L. Aballe, M. Belmeguenai, Y. Roussigné, S. Auffret, L. D. Buda-Prejbeanu, G. Gaudin, D. Ravelosona, and O. Boulle. Helium ions put magnetic skyrmions on the track. *Nano Lett.*, 21:2989–2996, 2021.
- [31] C. Reichhardt and C. J. Olson Reichhardt. Nonequilibrium phases for driven particle systems with effective orientational degrees of freedom. *Phys. Rev. E*, 79:061403, 2009.
- [32] C. Reichhardt and C. J. Olson Reichhardt. Statics and dynamics of Yukawa cluster crystals on ordered substrates. *Phys. Rev. E*, 85:051401, 2012.
- [33] S. Mühlbauer, B. Binz, F. Jonietz, C. Pfleiderer, A. Rosch, A. Neubauer, R. Georgii, and P. Böni. Skyrmion lattice in a chiral magnet. *Science*, 323(5916):915–919, 2009.
- [34] X. Z. Yu, Y. Onose, N. Kanazawa, J. H. Park, J. H. Han, Y. Matsui, N. Nagaosa, and Y. Tokura. Real-space observation of a two-dimensional skyrmion crystal. *Nature (London)*, 465(7300):901–904, 2010.
- [35] N. Nagaosa and Y. Tokura. Topological properties and dynamics of magnetic skyrmions. *Nature Nanotechnol.*, 8(12):899–911, 2013.
- [36] F. Jonietz, S. Mühlbauer, C. Pfleiderer, A. Neubauer, W. Münzer, A. Bauer, T. Adams, R. Georgii, P. Böni, R. A. Duine, K. Everschor, M. Garst, and A. Rosch. Spin transfer torques in MnSi at ultralow current densities. *Science*, 330(6011):1648–1651, 2010.
- [37] J. Iwasaki, M. Mochizuki, and N. Nagaosa. Universal current-velocity relation of skyrmion motion in chiral magnets. *Nature Commun.*, 4:1463, 2013.
- [38] C. Reichhardt, C. J. O. Reichhardt, and M. Milošević. Statics and dynamics of skyrmions interacting with disorder and nanostructures. *Rev. Mod. Phys.*, 94:035005, 2022.

- [39] K. Everschor-Sitte, J. Masell, R. M. Reeve, and M. Kläui. Perspective: Magnetic skyrmions - Overview of recent progress in an active research field. *J. Appl. Phys.*, 124(24):240901, 2018.
- [40] W. Jiang, X. Zhang, G. Yu, W. Zhang, X. Wang, M. B. Jungfleisch, J. E. Pearson, X. Cheng, O. Heinonen, K. L. Wang, Y. Zhou, A. Hoffmann, and S. G. E. te Velthuis. Direct observation of the skyrmion Hall effect. *Nature Phys.*, 13(2):162–169, 2017.
- [41] K. Litzius, I. Lemesh, B. Krüger, P. Bassirian, L. Caretta, K. Richter, F. Büttner, K. Sato, O. A. Tretiakov, J. Förster, R. M. Reeve, M. Weigand, I. Bykova, H. Stoll, G. Schütz, G. S. D. Beach, and M. Kläui. Skyrmion Hall effect revealed by direct time-resolved X-ray microscopy. *Nature Phys.*, 13(2):170–175, 2017.
- [42] R. Brearton, L. A. Turnbull, J. A. T. Verezhak, G. Balakrishnan, P. D. Hatton, G. van der Laan, and T. Hesjedal. Deriving the skyrmion Hall angle from skyrmion lattice dynamics. *Nature Commun.*, 12:2723, 2021.
- [43] C. Reichhardt and C. J. O. Reichhardt. Thermal creep and the skyrmion Hall angle in driven skyrmion crystals. *J. Phys.: Condens. Matter*, 31:07LT01, 2018.
- [44] C. Reichhardt, D. Ray, and C. J. O. Reichhardt. Nonequilibrium phases and segregation for skyrmions on periodic pinning arrays. *Phys. Rev. B*, 98:134418, 2018.
- [45] C. Reichhardt, D. Ray, and C. J. Olson Reichhardt. Quantized transport for a skyrmion moving on a two-dimensional periodic substrate. *Phys. Rev. B*, 91:104426, 2015.
- [46] N. P. Vizarim, C. Reichhardt, C. J. O. Reichhardt, and P. A. Venegas. Skyrmion dynamics and topological sorting on periodic obstacle arrays. *New J. Phys.*, 22:053025, 2020.
- [47] C. Reichhardt and F. Nori. Phase locking, devil’s staircases, Farey trees, and Arnold tongues in driven vortex lattices with periodic pinning. *Phys. Rev. Lett.*, 82:414–417, 1999.
- [48] P. T. Korda, M. B. Taylor, and D. G. Grier. Kinetically locked-in colloidal transport in an array of optical tweezers. *Phys. Rev. Lett.*, 89:128301, 2002.
- [49] M. P. MacDonald, G. C. Spalding, and K. Dholakia. Microfluidic sorting in an optical lattice. *Nature (London)*, 426:421–424, 2003.
- [50] X. Cao, E. Panizon, A. Vanossi, N. Manini, and C. Bechinger. Orientational and directional locking of colloidal clusters driven across periodic surfaces. *Nature Phys.*, 15(8):776, 2019.
- [51] N. P. Vizarim, C. Reichhardt, P. A. Venegas, and C. J. O. Reichhardt. Shapiro steps and nonlinear skyrmion Hall angles for dc and ac driven skyrmions on a two-dimensional periodic substrate. *Phys. Rev. B*, 102:104413, 2020.
- [52] J. C. B. Souza, N. P. Vizarim, C. J. O. Reichhardt, C. Reichhardt, and P. A. Venegas. Skyrmion soliton motion on periodic substrates by atomistic and particle-based simulations. *EPL*, 148(5):56002, 2024.
- [53] R. F. L. Evans. Atomistic Spin Dynamics. In W. Andreoni and S. Yip, editors, *Handbook of Materials Modeling: Applications: Current and Emerging Materials*, pages 1–23. Springer Nature Switzerland AG, 2018.
- [54] J. Iwasaki, M. Mochizuki, and N. Nagaosa. Current-induced skyrmion dynamics in constricted geometries. *Nature Nanotechnol.*, 8(10):742–747, 2013.
- [55] X. S. Wang, H. Y. Yuan, and X. R. Wang. A theory on skyrmion size. *Commun. Phys.*, 1:31, 2018.
- [56] S. Seki and M. Mochizuki. *Skyrmions in Magnetic Materials*. Springer, 2016.
- [57] T. L. Gilbert. A phenomenological theory of damping in ferromagnetic materials. *IEEE Trans. Mag.*, 40:3443–3449, 2004.
- [58] J. Zang, M. Mostovoy, J. H. Han, and N. Nagaosa. Dynamics of skyrmion crystals in metallic thin films. *Phys. Rev. Lett.*, 107:136804, 2011.
- [59] T. Schulz, R. Ritz, A. Bauer, M. Halder, M. Wagner, C. Franz, C. Pfeleiderer, K. Everschor, M. Garst, and A. Rosch. Emergent electrostatics of skyrmions in a chiral magnet. *Nature Phys.*, 8(4):301–304, 2012.
- [60] S.-Z. Lin, C. Reichhardt, C. D. Batista, and A. Saxena. Particle model for skyrmions in metallic chiral magnets: Dynamics, pinning, and creep. *Phys. Rev. B*, 87:214419, 2013.
- [61] J. Feilhauer, S. Saha, J. Tobik, M. Zelent, L. J. Heyderman, and M. Mrućkiewicz. Controlled motion of skyrmions in a magnetic antidot lattice. *Phys. Rev. B*, 102:184425, 2020.
- [62] See supplemental material for animations showing the different motions.